Chemical Geology 469 (2017) 129–146

Contents lists available at ScienceDirect

Chemical Geology

journal homepage: www.elsevier.com/locate/chemgeo

Geochemical characteristics of soil radon and carbon dioxide within the Dead Sea Fault and Karasu Fault in the Amik Basin (Hatay), Turkey

G. Yuce [a], C.C. Fu [b,*], W. D'Alessandro [c], A.H. Gulbay [a], C.W. Lai [d], S. Bellomo [c], T.F. Yang [d,1], F. Italiano [c], V. Walia [e]

[a] Hacettepe University, Department of Geological Engineering, Hydrogeology Division, Beytepe, 06800 Ankara, Turkey
[b] Institute of Earth Sciences, Academia Sinica, Taiwan
[c] Istituto Nazionale di Geofisica e Vulcanologia, Sezione di Palermo, Via Ugo La Malfa, 153, 90146 Palermo, Italy
[d] Department of Geosciences, National Taiwan University, Taipei, Taiwan
[e] National Center for Research on Earthquake Engineering, NARL, Taiwan

ARTICLE INFO

Article history:
Received 31 July 2016
Received in revised form 2 January 2017
Accepted 4 January 2017
Available online 15 January 2017

Keywords:
Dead Sea Fault
Karasu Fault
Amik Basin
Radon
Carbon dioxide

ABSTRACT

The study area is close to the boundary of three tectonic plates (Anatolian, Arabian, and African plates) and is characterized by important tectonic lineaments, which consist mainly of the Dead Sea Fault (DSF), the Karasu Fault, and the East Anatolian Fault (EAF) systems. To understand the origin of soil gas emanation and its relationships with the tectonics of the Amik Basin (Hatay), a detailed soil gas sampling was systematically performed. Together with CO_2 flux measurements, >220 soil gas samples were analyzed for Rn and CO_2 concentrations. The distribution of soil Rn (kBq/m^3), CO_2 concentration (ppm), and CO_2 flux (g/m^2/day) in the area appears as a point source (spot) and/or diffuses (halo) anomalies along the buried faults/fractures due to crustal leaks. The results revealed that Rn and CO_2 concentrations in the soil gas show anomalous values at the specific positions in the Amik Basin. The trace of these anomalous values is coincident with the N-S trending DSF. CO_2 is believed to act as a carrier for Rn gas. Based on the Rn and CO_2 concentrations of soil gases, at least three gas components are required to explain the observed variations. In addition to the atmospheric component, two other gas sources can be recognized. One is the deep crust component, which exhibits high Rn and CO_2 concentrations, and is considered the best indicator for the surface location of fault/fracture zones in the region. The other component is a shallower gas source with high Rn concentration and low CO_2 concentration. Moreover, He isotopic compositions of representative samples vary from 0.94 to 0.99 Ra, illustrating that most samples have a soil air component and may have mixed with some crustal component, without significant input of the mantle component. Based on the repeated measurements at a few sites, soil gas concentrations at the same site were observed to be higher in 2014 than in 2013, which may be associated with the activity of the DSF in 2013–2014. This suggests that soil gas variations at fault zone are closely related to the local crustal stress, and hence are suitable for monitoring fault activities.

1. Introduction

The Amik plain is located along the intersectional domain of several regional-scale structural lineaments, namely, the NE-SW trending sinistral East Anatolian Fault (EAF), the N-S trending sinistral Dead Sea Fault (DSF), and the NE-SW trending contractional Cyprus Arc (CA) (Fig. 1). The seismicity of the area has been widely archived throughout history. Several strong earthquakes have been recorded, such as the 1114, 1822, and 1872 earthquakes, which had magnitudes of ≥7 and resulted in severe casualties as well as property loss. To prevent possible hazards and disasters in the study area, the main objectives of this study were to better understand the distribution of active faults and gas emanation through soil gas investigations, and to assess the potential areas where earthquakes may occur.

Soil gas surveys have been performed to study a wide variety of different geological issues, including tectonic activities (Toutain et al., 1992; Ciotoli et al., 1998; Toutain and Baubron, 1999), fault exploration (Guerra and Lombardi, 2001; Baubron et al., 2002; Ioannides et al., 2003; Burton et al., 2004; Fu et al., 2005, 2008; Walia et al., 2005a, 2008, 2010; Inceoz et al., 2006; Lombardi and Voltattorni, 2010; Zhou et al., 2010), earthquakes and volcanic activity (King, 1980; Baubron et al., 1991; Virk and Singh, 1993; Al-Hilal and Mouty, 1994; King et al., 1996; Heiligmann et al., 1997; Chyi et al., 2005; Walia et al., 2005b, 2013; Yang et al., 2005b, 2006; Fu et al., 2009, 2015), exploration of petroleum, uranium mineralization, and geothermal reservoirs (Butt and Gole, 1986; Gole et al., 1986; Blunt and Fayers, 1993; Corazza et al.,

* Corresponding author.
E-mail address: ccfu@earth.sinica.edu.tw (C.C. Fu).
[1] Deceased.

http://dx.doi.org/10.1016/j.chemgeo.2017.01.003
0009-2541/

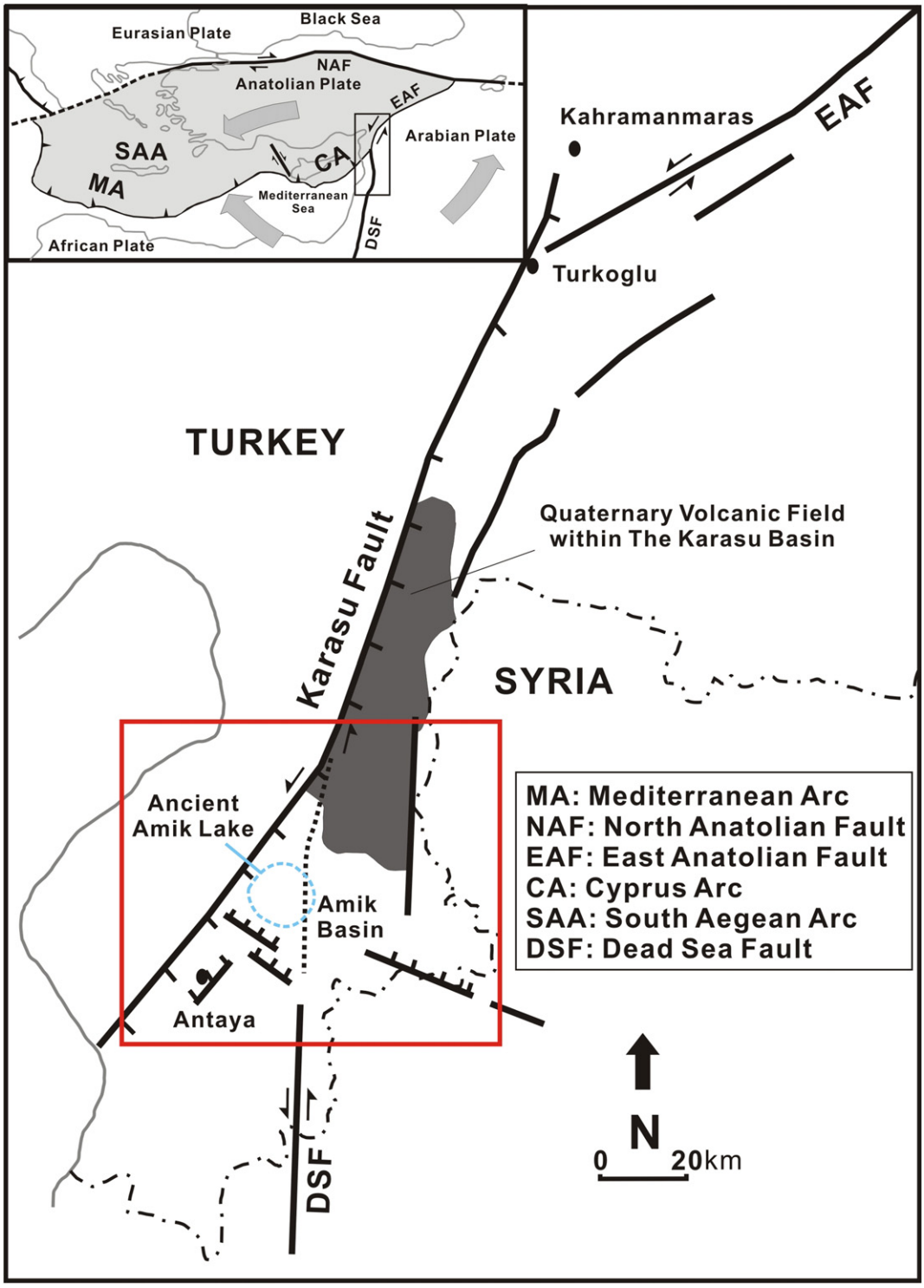

Fig. 1. A sketch map of the study area in the mainframe of the three tectonic plates. The simplified tectonic map of Turkey and the relative position of the research area are also indicated by the red rectangle.

1993; Belt and Rice, 2002; Phuong et al., 2012; Boyle, 2013), and the emission of greenhouse gases (D'Alessandro et al., 2009; Etiope, 2015).

The fundamental basis of gas geochemistry in application is that gases in the air and those derived from the deep crust and mantle have characteristic compositions that can be distinguished easily from one another. The deep crust- and mantle-derived gases usually exhibit higher concentrations of He, Rn, CO_2, and CH_4, which will diffuse or migrate together with the carrier gas toward the surface (Yang et al., 2003b; Hong et al., 2010) and mix with the air (Ciotoli et al., 1999; Tansi et al., 2005). Thus, soil gas compositions usually display mixed characteristics of air and deep source compositions. Gas migration can usually refer to the relationships between geodynamics and earth outgassing, and is related to the existence of gas sources and paths for degassing. The zones of enhanced permeability, such as faults and fractures that underlie the surface, allow gases to migrate upward from the deep. These gases can then be stored in the near-surface and provide information on deep sources (Astorri et al., 1999; Yang et al., 2003b; Swakon et al., 2005). Fu et al. (2005) found that concentrations of gas

species observed in the covering soil layers are highly affected by the soil types because of the variability of porosity. Some earlier investigations have revealed that soil gas concentrations may also be controlled by meteorological parameters, such as atmospheric pressure, humidity, temperature, and rainfall (e.g., Washington and Rose, 1992; Bunzl et al., 1998; Iakovleva and Ryzhakova, 2003). Therefore, it is necessary to eliminate possible meteorological effects when performing the soil gas survey. Furthermore, areas with a composition of sediment and soil with high permeability is the predominant type used for study (Bridgland et al., 2012). The pore space is expected to be filled with fluids and gases suitable for geochemical reconnaissance. Based on this concept, the soil gas technique is commonly adopted to explore unexposed fractures or blind faults that are unobservable at the surface.

Due to ascending strains, it is common for the mantle-derived gases to exhibit higher concentrations and a higher flux rate (Trique et al., 1999; Pulinets and Dunajecka, 2007). The study area, which is surrounded by the DSF and Karasu Fault in the Amik Basin (Hatay) where mantle-derived gases are still emanating, showed the presence of deep-rooted regional faults (Yuce et al., 2014). Here, we investigated the spatial patterns of soil gas compositions, and examined the association between the recent tectonic structure and degassing process. This paper accounts for the geochemical features of soil gas compositions from the southern border of the Amik Basin to the northern sector of the Karasu Fault zone, with the aim to obtain insight about the relationships with local tectonic settings and determine the buried fractures and active faults that cut through the basin.

2. Geological background

The study area is characterized by important tectonic structures, with the SW extension of the Karasu Fault connecting the DSF and EAF (Fig. 1). In this area, three plates meet to form an active triple junction (Mahmoud et al., 2005). The DSF accommodates the relative motion between the African (Sinai Block) and Arabian plates with sinistral strike-slip character (Freund et al., 1968; Hempton, 1987; Mahmoud et al., 2005). The DSF zone trends N-S from a sea-floor spreading center in the Red Sea in the south to the northern boundary of the Arabian plate, where the sinistral strike-slip EAF zone is reached. The DSF and EAF are linked to each other by the Karasu Fault, north of the Amik plain. The EAF zone, together with the North Anatolian Fault (NAF) zone, accommodates the westward extrusion of Anatolia, which is a response to the progressive collision of the Eurasian and African-Arabian plates (Sengör and Yilmaz, 1981; Saroglu et al., 1992). The Cyprus Arc (CA) to the south of Cyprus accommodates the convergence between the African and Anatolian plates in the region (Robertson, 1998). Based on the most recent earthquake data, the region is still seismically active, and originated from a NE-SW sinistral faulting with a normal dip-slip component in the Karasu Region (Erdik et al., 1997). The studies on slip rates based on subsurface geophysical data, GPS data, and field observations have suggested that the DSF zone branches in southern Turkey (e.g., Muehlberger, 1981) and that the S-N slip rate is partitioned (e.g., Chaimov and Barazangi, 1990). Based on the above investigations, there is a wide range of proposed slip rates, from 4 to 6 mm/year (Kuran, 1980; Kasapoglu, 1987; Yürür and Chorowicz, 1998; Kiratzi, 1993; Westaway, 1994), 1 to 6 mm/year (Rojay et al., 2001; Yurtmen et al., 2002; Westaway, 2004; Seyrek et al., 2007, Karabacak et al., 2010), to 3 to 11 mm/year (Quennell, 1958; McKenzie, 1972; Garfunkel, 1981; Kasapoglu, 1987; Meghraoui et al., 2003; Westaway, 2004; Gomez et al., 2007), for the EAF, Karasu Fault, and DSF, respectively.

The evolution of the Karasu Rift Valley (Antakya, SE Turkey) can be associated with the EAF, DSF, the transition zone between these two, or a combination of the three. The rift is interpreted as a pull-apart basin (Karabacak and Altunel, 2013), a half-graben resulting from flexural bend (Lyberis et al., 1992), a graben caused by the westward escape of the Anatolian plate (Yürür and Chorowicz, 1998), or a graben resulted from divergent strike-slip motion (Muehlberger, 1981; Rojay et al., 2001). The rift evolved in a contemporaneous transition from transpression to transtension with left lateral motions, which have rotated block-bounding faults in a clockwise rotation (Tatar et al., 2004). Fault slip results have indicated a sinistral strike-slip faulting in the Karasu Rift (Yürür and Chorowicz, 1998; Rojay et al., 2001; Tatar et al., 2004; Karabacak et al., 2010). The seismicity data have pointed out a tectonic model of crustal extension, while the GPS data have pointed to a transtensional model for the study area (Kiratzi, 1993; Barka and Reilinger, 1997; Reilinger et al., 1997, 2006; McClusky et al., 2000, 2003; Meghraoui et al., 2011).

2.1. Distribution of rock units

The stratigraphic units of the Antakya area evolved during the paleotectonic and neotectonic periods, and can be grouped into paleo- and neotectonic units, respectively. The closure of the northward subducting southern Tethys took place during the Late Cretaceous to the Miocene, which was the paleotectonic period in the area (the closure of the Bitlis-Zagros Ocean) (Sengör and Yilmaz, 1981). The Late Miocene neotectonic period was related to the propagation of the DSF and its linkage with the EAF zone.

The pre-Pliocene basement rocks are the major Paleotectonic units that can be classified into (a) Cretaceous ophiolite, (b) ophiolitic complex overthrusted onto pre-Cambrian to Campanian units, and (c) Campanian-Maastrichtian to Miocene extensive cover units. Cretaceous ophiolite and ophiolitic complexes have an extensive spatial distribution in the region and are composed of ultramafic tectonites, mafic and ultramafic cumulates, gabbros, sheeted dyke complexes, plagiogranites, pillow lava, bedded cherts, and pelagic limestones (Dilek and Thy, 2009). The Plio-Quaternary fluvial clastics and terraces deposited are observed only in subsidence areas such as Amik, Karasu, and Antakya during the neotectonic phase, and are not found on the elevated rift shoulders (Boulton et al., 2006). The Amik Basin sediments contain a fresh input of crystalline materials, notably local basalts, which are likely to be from the Precambrian/Palaeozoic. Coarser mafic rocks are probably derived from the latest Cretaceous Hatay ophiolite. However, it has been suggested that this area has been a subsiding sedimentary depocenter, due to the absence of any high ground, since the present geometry of the DSF zone in this region came into being for certain in the Mid Pliocene (Seyrek et al., 2007). Quaternary alkali basaltic volcanics are a product of the Neotectonic period (1.57 ± 0.08 to 0.05 ± 0.03 Ma), and are observed along the margins, center, and shoulders of the Karasu rift alternating with the Plio-Quaternary basin fill clastics (Çapan et al., 1987; Rojay et al., 2001) (Fig. 2). Based on a seismic reflection profile, Perinçek and Çemen (1990) indicated that the sedimentary fill in the Amik Basin reaches a maximum thickness of ~1 km.

3. Methodology

3.1. Sampling and analytical methods

Soil gas surveys were performed under similar dry seasons to avoid possible meteorological effects on the soil gas concentrations (Hinkle, 1994; Fu et al., 2005). Soil gas samples at 229 sites were systematically collected from the ca. 1–1.5 km spacing grid in the area during three field campaigns in August 2012, June 2013, and May 2014, and were analyzed for Rn and CO_2 concentrations, and CO_2 flux (Fig. 2). Table 1 shows the sample locations together with the gas concentrations and flux. In this study, the barometric pressure varied from 977 to 1008 mb, with an average of 994.2 mb and a standard deviation of 3.9 mb; atmospheric temperature varied from 29 to 45 °C, with an average of 36.2 °C and a standard deviation of 3.4 °C; and soil temperature varied from 25 to 44 °C, with an average of 34.2 °C and a standard deviation of 3.9 °C. The effects of meteorological parameters on CO_2 flux were evaluated (approximately <2%).

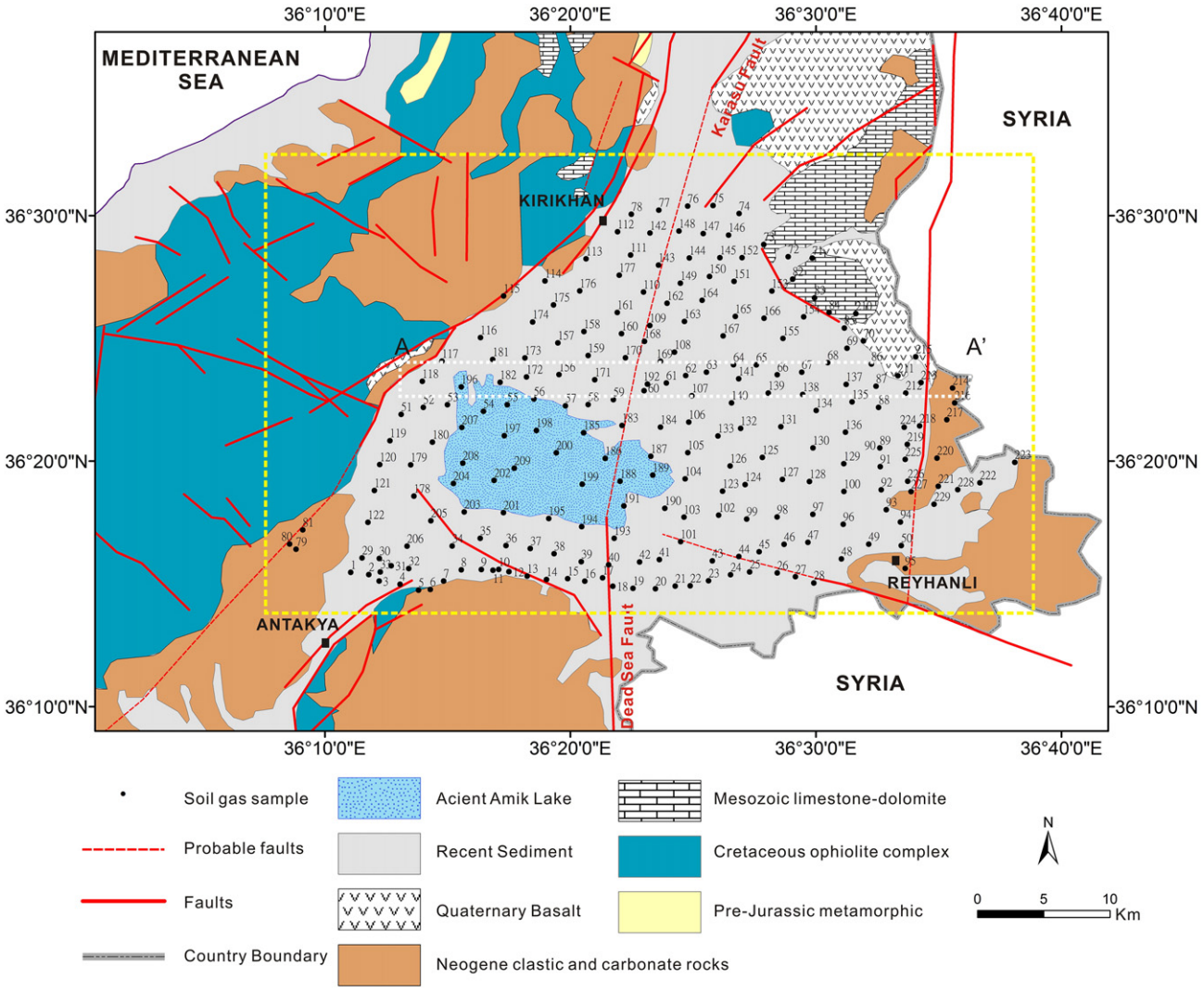

Fig. 2. Simplified geologic map with the soil gas sampling points. See Table 1 for sampling site details and coordinates.

A 130-cm long hollow steel probe of 1-cm outer and 0.7-cm inner diameters was driven into the ground at a depth of ~80 to 100 cm using a hammer on the probe's head. A disposable sharp awl was attached to the bottom of the steel probe to make it easier to drill into the soil and to prevent the probe from becoming blocked by soil. A thin solid billet inserted into the hollow steel probe was used to displace the awl, allowing the bottom of the probe to contact the soil at depth. A hand-pump was connected with a filtered rubber tube to prevent dust contamination. This tube was further connected to the hollow steel probe to suck out the existing air. The hand-pump was used to collect soil gas in the evacuated sample bag (3-liter capacity tedlar bag), for Rn concentration analysis. Rn is geochemically inert and the only radioactive noble gas with a half-life of 3.82 days. The calibration for Rn concentration was necessary to get the initial values ($Rn_{initial}$), using the following equation (Sensintaffar and Windham, 1990):

$$Rn_m = Rn_{initial}\, e^{-\lambda(t1-t0)} \quad (1)$$

where Rn_m is the measured concentration of Rn, λ is the decay constant of Rn (0.1813 d^{-1}), and t_0 and t_1 are the times between the collection and the analysis of the soil gas sample, respectively. The time of the period between sampling and analysis ranged from 0.3 to 21 h, with an average of 8.4 h. The Rn detector (RTM 2100, SARAD) has been used for the measurement of Rn concentration for many years (Walia et al., 2005a, 2008; Fu et al., 2008, 2009). The manufacturer has reported that the accuracy of measurement is better than ± 10%, and that the analytical limit of detection is ~30 Bq/m^3.

A few soil gas samples were collected in a vacuum sample bottle, which was made of potassium glass to preserve the helium gas from escaping by diffusion, for later He isotope analysis (Yang et al., 2005a). Helium, neon, and other noble gas concentrations and isotopic ratios in soil gas samples were directly analyzed from the sample bottles after purification in the high-vacuum inlet line of the noble gas mass spectrometer (Micromass 5400). The observed $^3He/^4He$ ratios were calibrated against atmospheric standard gas and were expressed relative to Ra, where Ra is the air $^3He/^4He$ ratio of 1.39×10^{-6} (Poreda and Craig, 1989). The overall error of the measured ratio, including the analytical errors of the sample and the working standard gas, and the long-term variations of the standard, was <2.5% (Yang et al., 2005a). Furthermore, the isotopic carbon ratios for CO_2 were analyzed with a Finnigan MAT mass spectrometer, after CO_2 purification under vacuum. Measured $^{13}C/^{12}C$ ratios are expressed as $\delta^{13}C$ values with respect to the V-PDB standard. The experimental error on the carbon isotopic ratios was ~0.1‰ (Capasso et al., 2005).

CO_2 concentrations and CO_2 flux measurements were performed on and near the Rn collecting sites, respectively. The measurements were carried out by IR LICOR (with a range of 0 to 20,000 ppm, accuracy of 2%) and Drager Polytron (with a range of 2000 ppm to 100%, accuracy of 3%), covering the concentration range from 1 ppm to 100% by volume. CO_2 concentrations in the soil were determined directly from the same

Table 1
A list of the date, site location, and composition of the soil gas samples collected in the Amik Basin area.

Sample ID	Date yyyy/m/dd	Long. (N)	Lat. (E)	Rn (kBq/m^3)	CO_2 (ppm)	CO_2 Flux ($g/m^2/day$)
1	2012/8/2	36.25785	36.18423	0.4	3920	0.8
2	2012/8/2	36.25632	36.19654	1.3	1100	0.8
3	2012/8/2	36.25191	36.20351	10.0	9860	1.1
4	2012/8/2	36.24977	36.21768	17.0	44,500	13.6
5	2012/8/2	36.24576	36.23031	33.8	5500	0.8
6	2012/8/3	36.24617	36.23823	6.0	5770	4.6
7	2012/8/3	36.25190	36.24733	3.1	4110	0.8
8	2012/8/3	36.25958	36.25926	3.0	7700	6.1
9	2012/8/4	36.25970	36.27288	6.7	4300	3.3
10	2012/8/4	36.25981	36.28473	6.5	–	8.6
11	2012/8/7	36.25923	36.28076	5.9	7450	8.0
12	2012/8/7	36.25828	36.29162	2.0	740	6.0
13	2012/8/7	36.25524	36.30405	4.1	5240	6.9
14	2012/8/7	36.25301	36.31715	5.7	10,400	0.8
15	2012/8/7	36.25353	36.33155	43.0	43,200	5.0
16	2012/8/7	36.25186	36.34312	12.0	43,700	10.8
17	2012/8/7	36.25407	36.35519	9.0	42,600	9.1
18	2012/8/7	36.24841	36.36219	29.0	19,700	0.8
19	2012/8/7	36.24695	36.37589	11.0	9820	6.3
20	2012/8/7	36.24671	36.39107	7.2	9800	0.8
21	2012/8/7	36.24853	36.40447	2.3	5150	0.8
22	2012/8/8	36.24871	36.41466	2.2	2900	1.9
23	2012/8/8	36.25211	36.42717	6.5	21,600	5.3
24	2012/8/8	36.25623	36.44206	3.3	4000	2.3
25	2012/8/8	36.25815	36.45499	15.6	11,400	0.8
26	2012/8/8	36.25744	36.47373	15.3	15,500	2.4
27	2012/8/8	36.25483	36.48612	10.7	35,400	2.5
28	2012/8/8	36.25063	36.49856	8.9	3420	0.8
29	2012/8/9	36.26765	36.19191	4.3	10,500	2.7
30	2012/8/9	36.26721	36.20362	1.4	41,700	6.3
31	2012/8/9	36.26229	36.21177	12.8	36,000	0.8
32	2012/8/9	36.26036	36.22363	10.5	28,700	0.8
33	2012/8/9	36.25815	36.20426	1.7	28,200	0.8
34	2012/8/10	36.27568	36.25315	11.7	5880	9.6
35	2012/8/10	36.28094	36.27212	14.3	5720	0.8
36	2012/8/10	36.27599	36.28966	41.1	65,500	11.8
37	2012/8/10	36.27398	36.30615	31.8	55,700	9.8
38	2012/8/10	36.27049	36.32231	33.1	67,000	6.1
39	2012/8/10	36.26507	36.34077	33.5	15,600	1.9
40	2012/8/10	36.26300	36.35929	19.0	25,800	2.8
41	2012/8/11	36.26646	36.39376	2.9	4050	0.8
42	2012/8/11	36.26482	36.38035	11.7	34,500	3.5
43	2012/8/11	36.26562	36.42968	5.3	36,400	0.8
44	2012/8/11	36.26855	36.44773	2.0	2250	0.8
45	2012/8/11	36.27184	36.46149	1.3	3240	1.7
46	2012/8/11	36.27683	36.47839	29.0	500	1.0
47	2012/8/11	36.27821	36.49461	2.7	2350	0.8
48	2012/8/12	36.26693	36.51732	35.2	38,700	5.9
49	2012/8/12	36.27692	36.53593	11.7	6900	3.2
50	2012/8/12	36.27595	36.55799	11.8	4750	0.8
51	2012/8/12	36.36503	36.21844	1.4	4370	1.1
52	2012/8/12	36.36985	36.23347	2.2	4620	0.8
53	2012/8/12	36.37165	36.24992	2.7	8240	10.0
54	2012/8/12	36.36716	36.27435	3.4	24,000	12.7
55	2012/8/13	36.37162	36.29055	8.8	18,400	8.6
56	2012/8/13	36.37549	36.30857	4.9	24,500	6.4
57	2012/8/13	36.37090	36.32998	3.7	24,000	5.2
58	2012/8/13	36.37176	36.34544	14.2	30,500	1.4
59	2012/8/13	36.37508	36.36258	6.7	8040	14.7
60	2012/8/13	36.38111	36.38335	19.1	39,000	0.8
61	2012/8/13	36.38636	36.39853	22.4	62,200	0.8
62	2012/8/13	36.39141	36.41163	5.3	6855	3.9
63	2012/8/13	36.39365	36.42575	12.1	25,100	0.8
64	2012/8/13	36.39871	36.44410	7.6	9400	1.0
65	2012/8/13	36.39865	36.45956	10.9	14,800	3.4
66	2012/8/14	36.39199	36.47380	3.6	2050	0.8
67	2012/8/14	36.39369	36.49044	19.7	120,700	3.0
68	2012/8/14	36.40015	36.50798	14.9	20,500	0.8
69	2012/8/14	36.40993	36.52117	5.4	25,800	1.9
70	2012/8/14	36.41487	36.53232	28.6	44,800	10.0
71	2012/8/14	36.47113	36.49760	27.7	6060	10.3
72	2012/8/14	36.47206	36.48120	51.1	183,000	0.8
73	2012/8/14	36.48041	36.46463	20.7	13,000	0.8

(continued on next page)

Table 1 (*continued*)

Sample ID	Date yyyy/m/dd	Long. (N)	Lat. (E)	Rn (kBq/m^3)	CO_2 (ppm)	CO_2 Flux (g/m^2/day)
74	2012/8/14	36.50137	36.44789	8.2	10,500	5.5
75	2012/8/14	36.50681	36.43022	4.7	5700	5.0
76	2012/8/14	36.50643	36.41295	10.5	11,100	3.9
77	2012/8/14	36.50373	36.39340	8.7	33,700	0.8
78	2012/8/14	36.50092	36.37476	3.3	13,700	24.1
79	2013/7/25	36.27353	36.14708	17.2	93,000	15.6
80	2013/7/25	36.27702	36.14272	18.7	28,300	1.0
81	2013/7/25	36.28661	36.15165	6.6	17,650	4.0
82	2013/7/27	36.45686	36.48423	31.0	25,560	11.5
83	2013/7/27	36.44416	36.49910	7.0	17,200	7.1
84	2013/7/27	36.43428	36.50901	22.4	23,500	9.8
85	2013/7/27	36.42369	36.51937	22.4	37,500	4.1
86	2013/7/27	36.39920	36.53771	4.5	10,000	14.9
87	2013/7/27	36.38422	36.54086	13.9	44,000	35.4
88	2013/7/27	36.36979	36.54261	0.4	1000	22.9
89	2013/7/27	36.34230	36.54338	3.2	2000	13.7
90	2013/7/27	36.34230	36.54338	15.8	22,600	2.1
91	2013/7/27	36.32952	36.54368	24.1	14,000	3.8
92	2013/7/27	36.31384	36.54440	15.5	9150	4.9
93	2013/7/27	36.30036	36.54779	7.8	7200	5.8
94	2013/7/27	36.29202	36.55744	2.2	1920	2.8
95	2013/7/27	36.26044	36.56067	59.6	11,000	9.9
96	2013/7/27	36.29047	36.51860	3.0	5200	2.7
97	2013/7/27	36.29724	36.49794	5.2	5300	1.7
98	2013/7/27	36.29536	36.47366	5.0	5100	14.2
99	2013/7/27	36.29396	36.45300	6.5	6800	9.7
100	2013/7/27	36.31270	36.51909	31.9	21,100	8.7
101	2013/7/28	36.27864	36.40825	11.5	6300	23.2
102	2013/7/28	36.29660	36.43402	1.9	7300	0.2
103	2013/7/28	36.29528	36.41046	1.6	5100	3.9
104	2013/7/28	36.32130	36.41124	1.8	4700	1.4
105	2013/7/28	36.33907	36.41307	2.6	2600	4.3
106	2013/7/28	36.35984	36.41373	0.3	8800	0.9
107	2013/7/28	36.37772	36.41587	3.9	1500	26.9
108	2013/7/28	36.40728	36.40403	0.6	6900	1.0
109	2013/7/28	36.42540	36.38725	3.2	1800	1.4
110	2013/7/28	36.44809	36.38296	23.0	1580	8.4
111	2013/7/28	36.47326	36.37427	5.5	39,500	9.7
112	2013/7/28	36.48899	36.36539	2.4	33,000	15.9
113	2013/7/28	36.47065	36.34396	14.8	7600	1.7
114	2013/7/28	36.45565	36.31610	7.1	55,000	11.4
115	2013/7/28	36.44546	36.28808	15.5	24,000	7.4
116	2013/7/28	36.41722	36.27231	3.8	20,500	3.0
117	2013/7/28	36.40117	36.24619	7.1	5800	7.9
118	2013/7/28	36.38752	36.23281	53.8	11,120	5.7
119	2013/7/28	36.34720	36.21083	2.5	12,250	8.6
120	2013/7/28	36.33098	36.20390	3.7	4000	3.9
121	2013/7/28	36.31335	36.20030	1.6	20,900	3.6
122	2013/7/28	36.29180	36.19595	0.6	13,900	1.8
123	2013/7/29	36.31293	36.43665	4.3	3000	5.7
124	2013/7/29	36.31742	36.45199	1.5	11,400	4.9
125	2013/7/29	36.33587	36.46373	0.3	3900	5.7
126	2013/7/29	36.33001	36.44181	13.1	12,000	6.9
127	2013/7/29	36.32088	36.47731	7.0	12,400	5.8
128	2013/7/29	36.31948	36.49563	10.9	5200	3.2
129	2013/7/29	36.33154	36.51901	9.7	7850	18.2
130	2013/7/29	36.34234	36.49799	25.4	22,650	12.2
131	2013/7/29	36.35670	36.47623	14.7	19,700	15.5
132	2013/7/29	36.35551	36.44890	21.8	36,800	14.2
133	2013/7/29	36.35044	36.43348	8.5	19,200	14.3
134	2013/7/29	36.36768	36.50022	11.3	2350	12.1
135	2013/7/29	36.37350	36.52456	7.3	16,430	5.4
136	2013/7/29	36.35297	36.52009	13.1	9100	19.8
137	2013/7/29	36.38546	36.52055	15.6	33,333	6.1
138	2013/7/29	36.37858	36.49107	15.2	15,650	8.9
139	2013/7/29	36.37952	36.46764	9.6	6100	7.4
140	2013/7/29	36.37282	36.44279	11.8	32,100	1.7
141	2013/7/29	36.38921	36.44757	14.0	18,000	35.9
142	2013/7/30	36.48819	36.38737	4.2	16,400	31.0
143	2013/7/30	36.46635	36.39322	3.8	29,500	6.4
144	2013/7/30	36.47123	36.41414	3.9	14,300	10.4
145	2013/7/30	36.47139	36.43486	11.4	6000	11.9
146	2013/7/30	36.48679	36.44076	26.1	25,700	15.5
147	2013/7/30	36.48783	36.42351	29.1	23,490	8.0
148	2013/7/30	36.48951	36.40707	51.8	47,000	2.7

Table 1 (*continued*)

Sample ID	Date yyyy/m/dd	Long. (N)	Lat. (E)	Rn (kBq/m^3)	CO_2 (ppm)	CO_2 Flux ($g/m^2/day$)
149	2013/7/30	36.45409	36.40801	0.9	2500	9.4
150	2013/7/30	36.45873	36.42781	16.3	13,000	8.1
151	2013/7/30	36.45538	36.44445	2.8	17,500	0.2
152	2013/7/30	36.47144	36.44985	8.9	4300	0.9
153	2013/7/30	36.44879	36.47011	12.7	6350	7.9
154	2013/7/30	36.43130	36.49175	16.8	31,200	4.9
155	2013/7/30	36.41661	36.47770	17.8	36,000	15.4
156	2013/7/31	36.39205	36.32566	16.3	44,300	11.5
157	2013/7/31	36.41360	36.32490	7.4	14,350	13.2
158	2013/7/31	36.42127	36.34253	17.2	23,000	11.5
159	2013/7/31	36.40503	36.34542	8.3	22,600	23.3
160	2013/7/31	36.41985	36.36808	2.6	11,300	15.6
161	2013/7/31	36.43427	36.36520	5.3	7000	2.3
162	2013/7/31	36.44048	36.39897	0.7	770	10.7
163	2013/7/31	36.42812	36.41080	3.5	5000	4.8
164	2013/7/31	36.44249	36.42279	10.3	26,900	10.4
165	2013/7/31	36.43158	36.44528	11.4	39,700	19.6
166	2013/7/31	36.43034	36.46487	3.1	12,700	10.1
167	2013/7/31	36.41837	36.43702	1.0	3000	7.1
168	2013/7/31	36.41466	36.38367	0.7	1650	3.7
169	2013/7/31	36.40112	36.39455	10.6	15,000	8.5
170	2013/7/31	36.40348	36.37077	4.8	12,200	6.7
171	2013/7/31	36.38854	36.34987	0.6	1850	8.6
172	2013/7/31	36.39044	36.30356	18.1	56,000	4.7
173	2013/7/31	36.40339	36.30252	6.7	21,500	3.6
174	2013/7/31	36.42780	36.30769	2.6	3700	–
175	2013/7/31	36.43932	36.32195	2.8	5300	9.7
176	2013/7/31	36.44885	36.33968	0.7	2300	4.3
177	2013/7/31	36.45953	36.36649	0.5	830	7.3
178	2013/8/1	36.30956	36.22718	2.9	16,600	1.7
179	2013/8/1	36.33083	36.22496	2.1	4000	4.1
180	2013/8/1	36.34623	36.23969	2.1	8650	4.3
181	2013/8/1	36.40231	36.28063	0.5	2100	20.4
182	2013/8/1	36.38685	36.28562	1.4	3000	5.9
183	2013/8/1	36.35758	36.36845	0.7	2000	2.1
184	2013/8/1	36.35637	36.39454	0.4	1850	8.7
185	2013/8/1	36.35260	36.34241	6.4	6400	16.5
186	2013/8/1	36.33514	36.35701	5.9	21,100	8.2
187	2013/8/1	36.33659	36.38799	0.5	21,430	24.3
188	2013/8/1	36.31969	36.36709	12.9	69,000	11.1
189	2013/8/1	36.32381	36.38927	12.9	36,700	30.3
190	2013/8/1	36.30131	36.39747	0.7	2250	4.4
191	2013/8/1	36.30291	36.36972	1.0	820	–
192	2013/8/1	36.38565	36.38565	1.0	3000	50.3
193	2013/8/1	36.28092	36.36312	1.0	2500	4.1
194	2013/8/1	36.28883	36.34099	1.4	3800	27.6
195	2013/8/1	36.29433	36.31865	3.2	8000	–
196	2013/8/2	36.38369	36.25928	1.5	9000	4.9
197	2013/8/2	36.35057	36.28848	1.3	4400	2.0
198	2013/8/2	36.35416	36.31026	6.6	28,000	4.8
199	2013/8/2	36.31768	36.34142	16.5	15,600	16.4
200	2013/8/2	36.33896	36.32378	7.5	28,800	1.6
201	2013/8/2	36.29836	36.28798	4.2	3000	2.0
202	2013/8/2	36.32026	36.28155	1.6	7600	7.0
203	2013/8/2	36.29887	36.26129	0.9	4200	–
204	2013/8/2	36.31811	36.25394	4.1	2400	12.6
205	2013/8/2	36.29288	36.23866	0.6	2500	–
206	2013/8/2	36.27563	36.22248	8.5	27,500	3.5
207	2014/5/13	36.35617	36.25967	1.5	6770	5.4
208	2014/5/13	36.33195	36.26032	19.2	25,300	5.7
209	2014/5/13	36.32849	36.29528	4.7	7200	4.4
210	2014/5/15	36.43351	36.52712	16.8	11,300	5.6
211	2014/5/15	36.39131	36.55572	10.8	4700	6.0
212	2014/5/15	36.37956	36.56102	13.2	7255	1.9
213	2014/5/15	36.38666	36.57135	14.2	8280	7.3
214	2014/5/15	36.38291	36.59279	31.6	6400	5.3
215	2014/5/15	36.40413	36.56781	18.7	8400	29.6
216	2014/5/15	36.37287	36.59420	83.9	11,000	0.9
217	2014/5/15	36.36142	36.58893	29.6	5200	16.6
218	2014/5/16	36.35728	36.57041	14.7	10,980	12.1
219	2014/5/16	36.34470	36.56211	11.4	10,000	10.2
220	2014/5/16	36.33534	36.58228	4.9	6400	7.1
221	2014/5/16	36.31623	36.58312	5.2	2780	20.6
222	2014/5/16	36.31865	36.61131	19.1	9700	2.0

(*continued on next page*)

Table 1 (*continued*)

Sample ID	Date yyyy/m/dd	Long. (N)	Lat. (E)	Rn (kBq/m^3)	CO_2 (ppm)	CO_2 Flux (g/m^2/day)
223	2014/5/16	36.33256	36.63502	2.9	1600	5.0
224	2014/5/16	36.35634	36.55997	14.3	10,000	5.0
225	2014/5/16	36.33451	36.56066	12.0	4160	25.0
226	2014/5/16	36.31968	36.56235	14.6	4800	–
227	2014/5/16	36.31259	36.56464	7.6	1400	3.8
228	2014/5/16	36.31398	36.59635	3.4	3920	55.4
229	2014/5/16	36.30403	36.58026	35.9	31,600	–

Table 2
Main statistical parameters of Rn concentration, CO_2 concentration, and CO_2 flux measured in the Amik Basin area.

	N	Mean	Median	SD	LQ	UQ	IQR	Min	Max	Anomaly threshold
Rn (kBq/m^3)	229	11.2	7.3	12.0	2.9	14.8	11.9	0.25	83.9	17
CO_2 (ppm)	229	16,812	9930	20,101	4700	24,000	19,300	500	183,000	40,000
CO_2 flux (g/m^2/day)	228	7.8	5.5	8.2	2.1	10.8	8.7	0.18	55.4	16

hollow steel probe that was used for Rn analysis, by injecting 100 ml of soil gas directly in the IR LICOR and Drager Polytron detector. CO_2 flux measurements from the surface were performed with a closed-chamber system (West Systems, Italy). An inlet and an outlet made the system a circular loop. A capillary was assembled to the top of the chamber to balance pressure. A fan was equipped in the chamber to ensure that air and soil gas were well-mixed. The CO_2 flux was calculated through a linear regression of the gas concentration build-up in the chamber. The details of the closed-chamber method were described by Chiodini et al. (1998). Soil temperature and atmospheric pressure were also recorded at each measurement to convert ppm/s to g/m^2/day as the unit of soil CO_2 flux values. The rate of increase in CO_2 concentration in the chamber (dc/dt) was computed for soil CO_2 flux (F), expressed in g/m^2/day, using the following equation:

$$F = k(V/S)(P/T)(dc/dt) \quad (2)$$

where k is the gas constant, V is the container volume (m^3), S is the surface area of the chamber base (m^2), P is the atmospheric pressure in Pa, and T is the measured soil temperature in K. A conservative estimate of the systematic uncertainty of this method is ~10% (Chiodini et al., 1998).

4. Results and discussion

A detailed soil gas survey throughout the Amik Basin area was carried out to compare soil gas trends with the results of the structural data (Fig. 2). The results revealed that concentrations vary in a wide range among all sampling sites: Rn ranged from 0.25 to 83.9 kBq/m^3; CO_2 from 500 to 183,000 ppm; and CO_2 flux from 0.18 to 55.4 g/m^2/d. These values, especially for Rn, are generally higher than the air composition (Rn < 100 Bq/m^3, CO_2 ~400 ppm according to https://www.co2.earth), indicating that the degree of contamination by air is small (Tables 1 and 2).

4.1. Recognition of anomalous concentrations

Descriptive statistics of soil gas measurements are reported in Table 2 and are also shown as box plots in Fig. 3. Due to their complex origins and sources, as well as their relative abundance with respect to atmospheric air, soil gas anomaly thresholds cannot be absolutely fixed. Many methods have been used to estimate the threshold values. In some cases, the interquartile range (IQR) highlights values that may be considered anomalous (Beaubien et al., 2003; Ciotoli et al., 2007). Threshold values can also be determined using the mean values plus two standard deviations after trimming off the anomalously high values (Baubron et al., 2002; Fu et al., 2005). However, the importance of threshold value estimation is related to recognizing the limit between background values caused by many parameters such as local gas productions, rock formations, and soil types, and anomalous concentrations connected to gas migration along the fault/fracture.

The aforementioned methods aside, the background level of soil gas in this study was assessed based on quantile-quantile plot (QQ Plot)

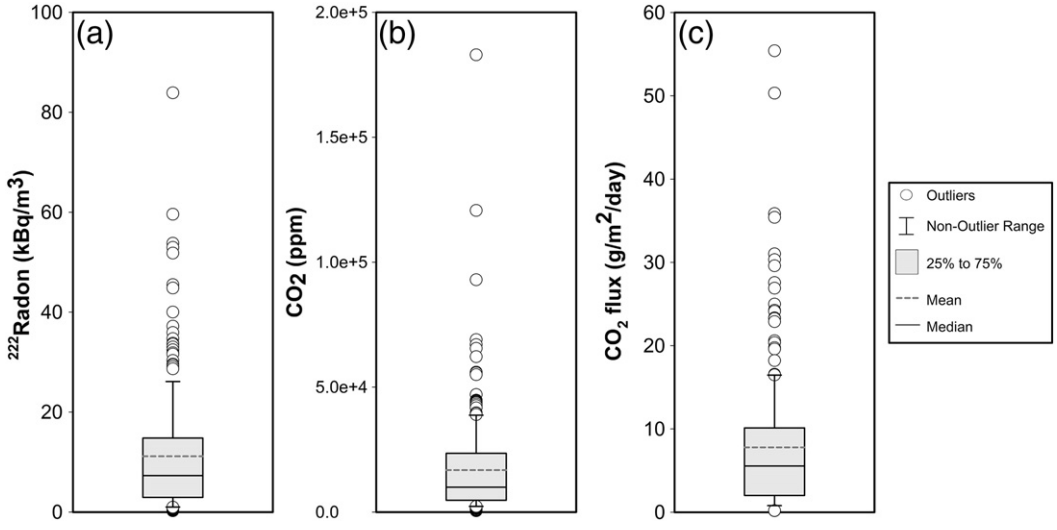

Fig. 3. Box plots of the different soil gas species (Rn concentration, CO_2 concentration, and CO_2 flux) in the Amik Basin based on >220 samples collected during three surveys.

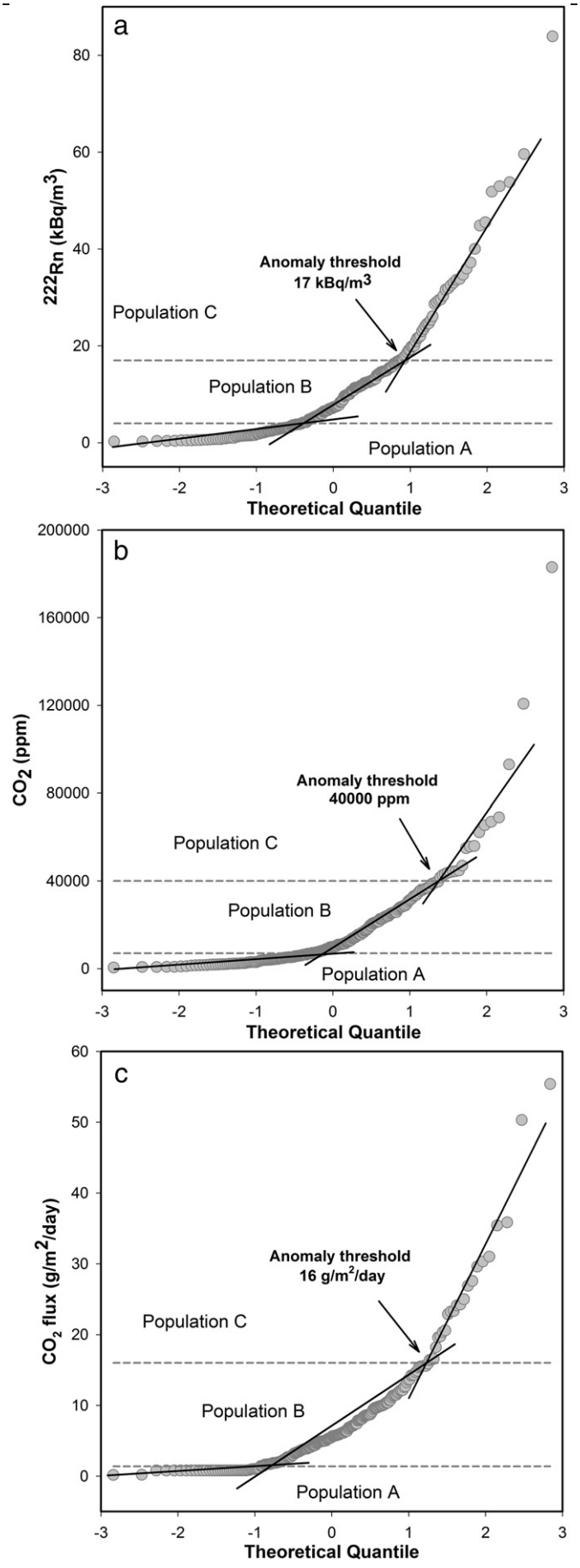

analysis, which is a useful method for distinguishing different populations between background and anomalous values (Kafadar and Spiegelman, 1986; Cheng et al., 1994). Here, we have adopted values derived from the QQ plot method based on a more sophisticated statistic derivation. The gas anomaly thresholds were determined on the basis of QQ plots by approximating segments of a straight line, and then choosing values at abscissa levels that correspond to the intersections of these linear segments. The resultant threshold values for anomalous signals were 17 kBq/m^3 for Rn, 40,000 ppm for CO_2, and 16 g/m^2/d for CO_2 flux, respectively (Fig. 4). On this basis, soil gas concentrations higher than the threshold value (population C) are depicted as different symbols, and intermediate high values (population B) and background values (population A) in soil gas concentrations are also included (Fig. 5a–d). Further, using the SURFER software (e.g., Fu et al., 2008), contour maps for Rn concentration, CO_2 concentration, and CO_2 flux were constructed (Fig. 6a–c) through Kriging interpolation to compare the distribution of soil gas anomalies (Fig. 5).

4.2. Spatial variations of soil gases

Reconnaissance of soil gas variations in space is also used to better understand the trace of targeted fault zones. This is based on the proposition that fault zones usually exhibit a higher carrier gas flux, and thus a higher concentration of rare gases (Etiope and Lombardi, 1995; Yang et al., 2003b). Classed post maps of Rn concentration, CO_2 concentration, and CO_2 flux were constructed using anomaly thresholds for separate concentration groups (Fig. 5). Based on the results shown in Fig. 5, we first examined the relationship between the anomalies of soil gases (Rn and CO_2 concentrations and CO_2 flux) and traces of the DSF and the Karasu Fault to assess if soil gas concentrations can be used as potential indicators to define faults in the study area. When the highest population values (i.e., when population C is higher than threshold values for Rn, CO_2, and CO_2 flux) are considered, it may be inferred that those sites may be the surface trace of faults/fractures zone in this area (Fig. 5d), which is consistent with the present (main) fault traces on the map shown by solid line (Fig. 2). That is, some parts of the lineation have already been previously determined by tectonic studies; however, there is a gap between both ends of the fault line, due to the inclination of both fault planes proposing the ~1.5-km shift of fault traces from the present location (please refer to the full line in Fig. 2).

When compared to the fault lines established in the Amik Basin area, we found that five, five, and two sites with anomalous Rn concentration, CO_2 concentration, and CO_2 flux, respectively, showed high concentrations near the trace of the N-S trending DSF (within 2.5 km). However, three, two, and one sites that have anomalous Rn concentration, CO_2 concentration, and CO_2 flux, respectively, showed high concentrations near the NE-SW trending Karasu Fault. Similar to the Rn concentration (Fig. 6a), CO_2 concentration (Fig. 6b), and CO_2 flux (Fig. 6c) contour maps, the higher soil gas values were also concentrated near the DSF and Karasu Fault.

The classed post maps also show the clear alignments of anomalous values in the northeastern and southwestern borders of the Amik Basin, which coincide with the structural setting of the study area. These patterns are likely not only caused by shallow sources such as organic matter decomposition, root respiration, rock weathering, and meteorological parameters, because the distribution of these gases is not homogenous (Ciotoli et al., 2014). That is, the family in Fig. 6 typically shows a halo anomaly. Furthermore, in Fig. 6a, a spot anomaly is identified in the northwest of the Amik Basin, while a halo anomaly is seen

Fig. 4. Quantile-quantile plots of calculated soil gas measurements for (a) Rn concentration, (b) CO_2 concentration, and (c) CO_2 flux. The anomaly threshold values are indicated as follows: (a) 17 kBq/m^3 for Rn, (b) 40,000 ppm for CO_2, and (c) 16 g/m^2/d for CO_2. This plot indicates that the soil gas data are separated into different populations recognizable by the inflection point on the curve. Population A presents the background values; Population C shows high anomalies; Population B occupies the mixing characteristics of Populations A and C.

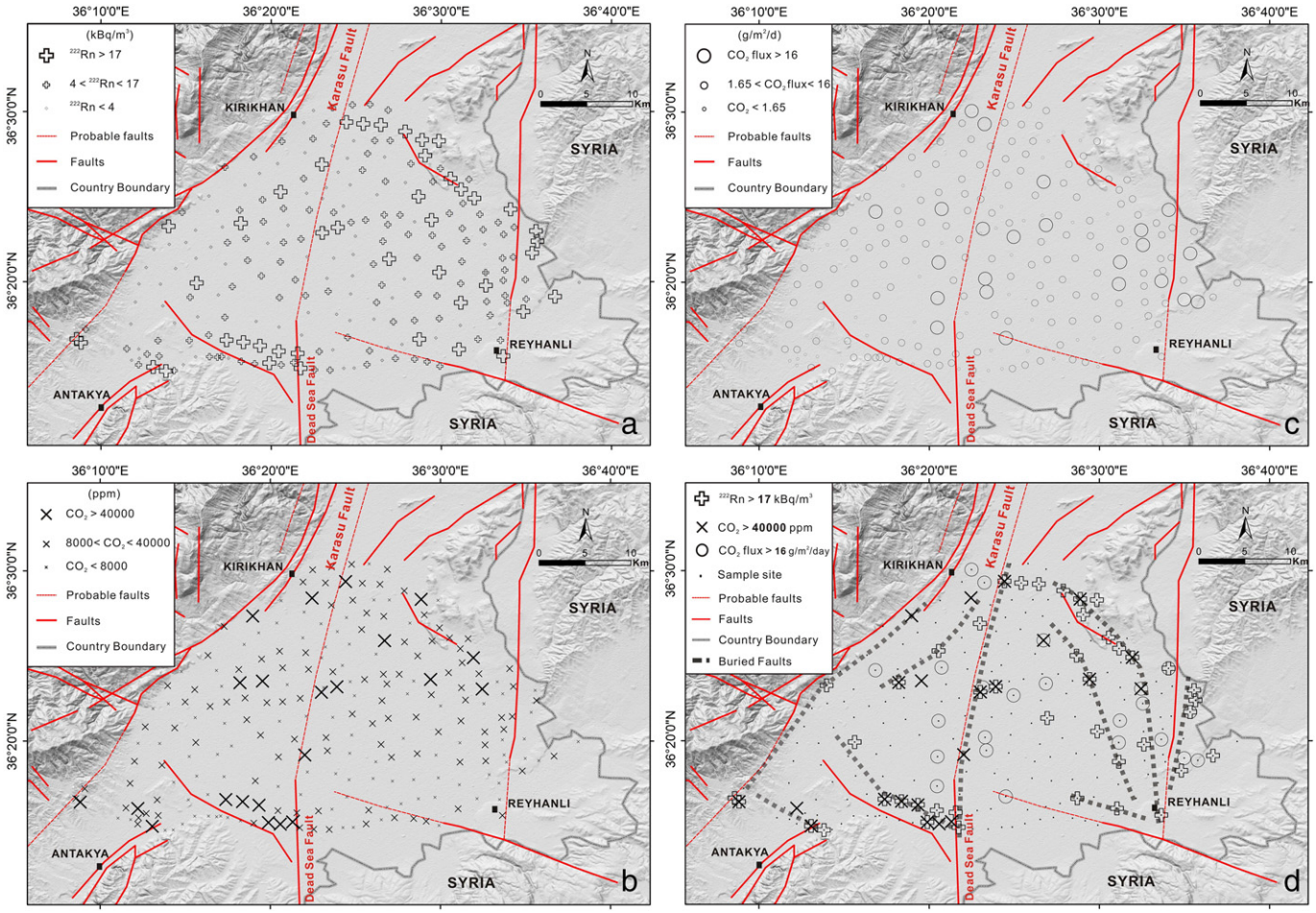

Fig. 5. Classed post maps showing the results of soil gas measurements for (a) Rn concentration, (b) CO_2 concentration, (c) CO_2 flux, and (d) anomalous values of gas concentrations and flux. The grey dashed lines indicate the possible buried faults and/or fractures recognized by the distribution of soil gas anomalies.

northeast of the Amik Basin. This is due to the heterogeneity of porosity and permeability, or because more fractures are present in the northeast. Karabacak and Altunel (2013) proposed that the slip of the DSF was transferred toward the north by the Karasu Fault in the Amik Basin. The left step-over on the left-lateral fault zone resulted in subsidence between the DSF and Karasu Fault, suggesting that the Amik Basin initially formed as a pull-apart basin. Based on the physical modeling of a pull-apart basin, Dooley and McClay (1997) and Rodgers (1980) considered that the two segments of the strike-slip fault resulted in the deformation of a basin. The normal faults were developed along the flank of a pull-apart basin during the deformation with lateral motion on the strike-slip fault system in an extensional setting such as the Amik Basin and the Ghab Basin. Therefore, the anomalous values in the northeastern and southwestern margins of the Amik Basin could be caused by the crustal deformation along the DSF, which induced changes in permeability within these zones of normal faulting (Fig. 5). Similar to the contour maps of soil gas, the higher soil gas values showed the NW-SE trend along the northeastern and southwestern Amik Basin, especially for Rn concentration (Fig. 6a) and CO_2 concentration (Fig. 6b).

However, a slight difference of Rn concentration in different rock units was observed. For example, for Mesozoic limestone-dolomite (sites 71, 73, 82, 83, 84, and 210; Fig. 2), Rn ranged from 7 to 30.98 kBq/m^3, with an average value of 20.9 kBq/m^3; for Neogene clastic and carbonate rocks (sites 79, 80, 81, 95, 115, 214, 216, 217, 220, 221, and 227; Fig. 2), Rn ranged from 4.85 to 83.9 kBq/m^3, with an average value of 24.6 kBq/m^3; for the Ancient Amik Lake area, Rn ranged from 0.49 to 31.8 kBq/m^3, with an average value of 7.7 kBq/m^3 (Fig. 2); for recent sediment, Rn ranged from 0.25 to 59.6 kBq/m^3, with an average value of 10.4 kBq/m^3 (Fig. 2). Such differences suggest that rock type may also play a role in the effect of Rn concentration in this study (El-Arabi et al., 2006).

It is of particular interest that the higher soil gas values are widely observed in the eastern Amik Basin (Figs. 5 and 6), which suggests that the enhanced permeability belt prevails between the DSF and the eastern border of the Amik Basin. This zone of anomalous values may imply the presence of faults, as a result of the propagation of the DSF splaying into different branches toward the surface (Karabacak et al., 2010). Due to the sediment deposition of over 1-km thickness in the western Amik Basin, gases are unlikely to migrate to the surface from deep sources because of the variability of porosity. Similarly, Fu et al. (2005) reported that soil gas concentrations of gas species observed in the covering soil layers are highly affected by soil porosity.

4.3. Temporal variations of soil gases

The anomaly zones determined may be gas geochemistry-sensitive and suitable for the soil gas monitoring of earthquake precursors (Chyi et al., 2001; Fu et al., 2008; Inan et al., 2008). A sensitive site on the study area, as evidenced by high concentrations in both major and trace gases, was chosen for long-term monitoring. To understand the relationship between temporal variations of the soil concentration and seismic/crustal activity in this area, 13 samples at the same site were collected during 2013 and 2014, and the results are shown in Fig. 7. Some substantial enhancements of the Rn concentration and CO_2 flux were observed, and a slight increase in CO_2 concentration can also be found; the rise of gas compositions on the eastern side of the DSF was

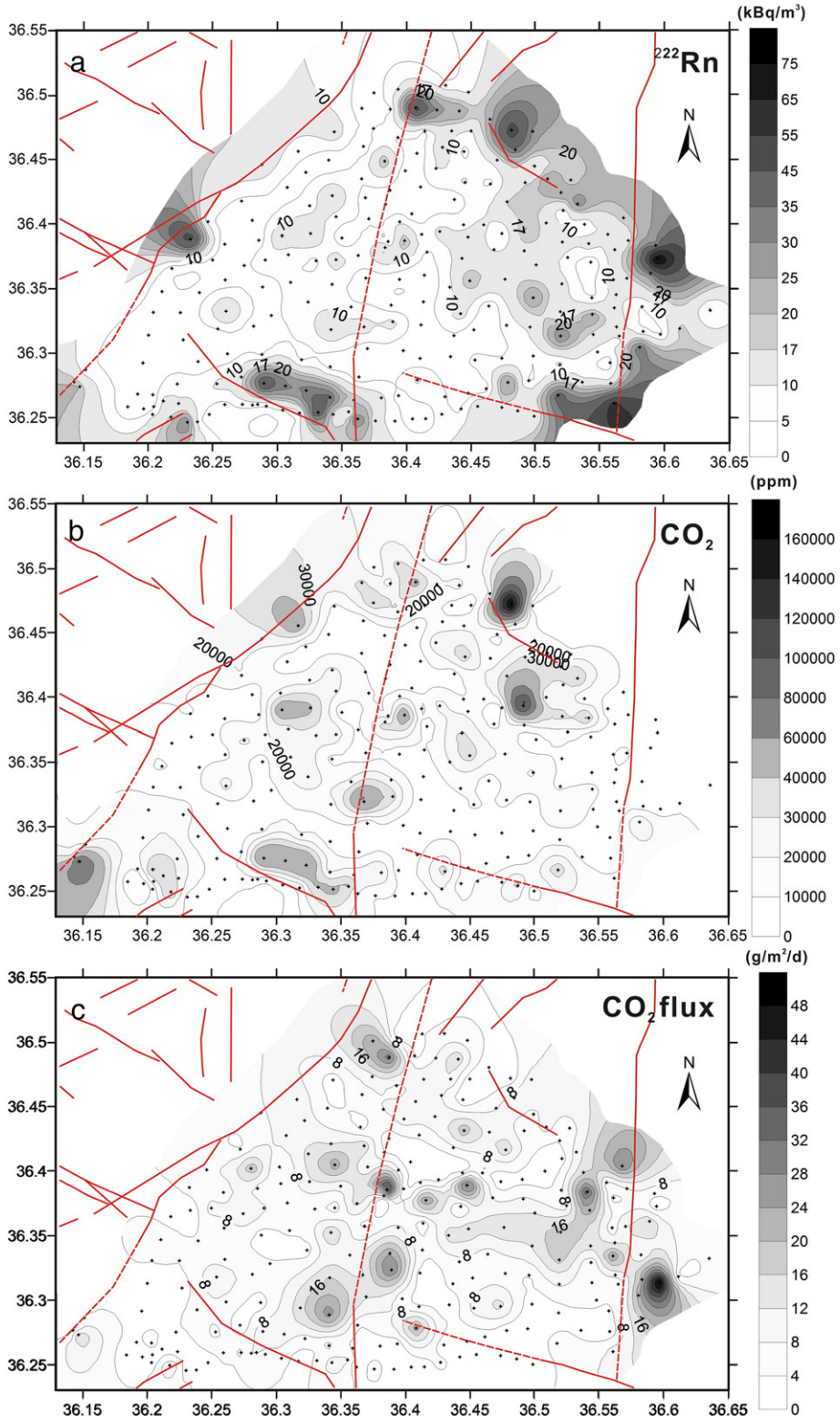

Fig. 6. Contour maps of (a) Rn concentration, (b) CO_2 concentration, and (c) CO_2 flux in the Amik Basin. Dot symbols indicate the sampling site for the soil gas survey in this study. The relative position of the contour map region is marked by a rectangle in Fig. 2.

especially conspicuous (e.g., site 149, greater than a 100% increase). Furthermore, the anomalous high soil gas values almost occurred close to the DSF zone (relative distance from the DSF to the sample site). The barometric pressure varied from 993 to 1007 mb with a standard deviation of 3.9 mb in 2013, and 1003 to 1008 mb with a standard deviation of 1.4 mb in 2014; atmospheric temperature varied from 33 to 45 °C with a standard deviation of 3.4 °C in 2013, and 22 to 26 °C with a standard deviation of 1.1 °C in 2014. The atmospheric disturbance in 2013 and 2014 was relatively small and may have influenced only approximately <2% of the soil flux.

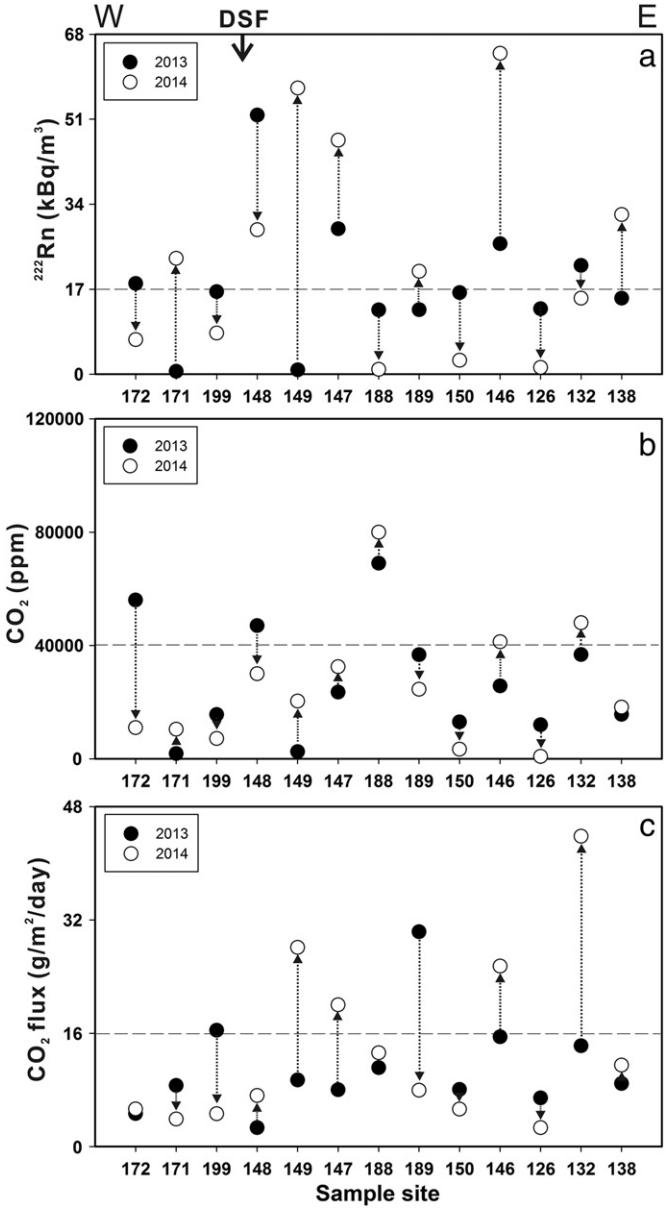

Fig. 7. Comparison of the repeated soil Rn concentration, CO_2 concentration, and CO_2 flux measurements in 2013 and 2014. The dashed line indicates the anomaly threshold of soil gas (see Fig. 4). The relative positions of the sampling sites are shown in Fig. 2.

Furthermore, due to the insufficient network for earthquake activities, the number and intensity of detectable earthquakes are low in the area, and no significant large seismic event was recorded before and after the sampling period. Therefore, seismicity may not be a major inference of soil gas changes. Since the effect of meteorological factors has been ruled out based on sampling during the dry season without precipitation, the increase in soil gas may have been caused by crustal deformation that was induced by changes in permeability, which suggests that the DSF is still active. However, the reason for some decreases in soil gases is still not clear.

The emission of soil CO_2 was estimated by averaging the contribution of each population. The results are 0.8 ± 0.3 g/m^2/d, 6.9 ± 3.8 g/m^2/d, and 26.7 ± 9.9 g/m^2/d for population A, population B, and population C, respectively. The CO_2 flux of the DSF is relatively smaller than that of some of the active tectonic locations of the world (Table 3). This suggests that the lower CO_2 flux may be associated with a larger sediment fill in the Amik Basin of the study area. However, the CO_2 of population C is still even higher than that of the San Andreas and Chukuo faults (Lewicki et al., 2003; Cheng, 2009). It is worth having a continuous sampling that will allow us to better understand the relationship between soil gas variations and regional geodynamic processes in the area.

4.4. Sources of the soil gases and the relationship between the tectonic setting and the mechanism of gas/fluid migration

Some trace gases in the Earth can migrate to the surface from deep sources together with other gases (e.g., CO_2, N_2, and CH_4) known as the carrier gases (Etiope and Martinelli, 2002; Yang et al., 2003b). As shown in Fig. 8, in addition to air component "A", which is the dominant source for soil gas, two other end components can be identified. One is deep source component "B", in which Rn is carried by CO_2 so that radon concentrations rise as CO_2 concentrations increase. Another is shallow source component "C", in which Rn concentrations do not show distinct variation as CO_2 concentrations increase. This is evidence that soil CO_2 in the region originates from both shallow and deep components. Carbon isotopic data for CO_2 in four samples (sites 4, 17, 37, and 38) ranged from −15.6 to −20.1‰. These $\delta^{13}C_{CO_2}$ values show that CO_2 gas in the study area may be explained as the result of mixing between organic sediments (ca. −30‰) and limestone (0‰) components (Hoefs, 2004).

He and its isotopes are excellent natural tracers for elucidating mantle-crust interactions in different geotectonic provinces, because it is chemically inert and characterized by negligible isotopic fractionation during gas-water-rock interaction processes. Distinct mantle, crustal, and atmospheric sources are characterized by unique He isotopic compositions, so their sources can be identified and used to constrain the history of the fluid. Continental crust with negligible additions of mantle volatiles has low $^3He/^4He$ ratios of 0.01 to 0.05 R_A, reflecting a strong radiogenic ^4He component. The upper asthenosphere, as constrained by samples of mid-ocean ridge basalt (MORB), has a $^3He/^4He$ ratio of 8 ± 1 R_A that indicates the presence of primordial ^3He acquired during the Earth's formation (Ballentine et al., 2002).

The presence of a significant mantle signature of He has often been used to track the input of mantle fluids in the crust through either the injection of magma batches (Sano and Wakita, 1985; Yang et al., 2003a) or along deep-rooted regional transform faults. Examples of the latter mechanism can be found in Turkey along the NAF (Gülec et al., 2002) and the EAF (Italiano et al., 2013), in Greece (D'Alessandro et al., 2014), in California at the San Andreas Fault (Kulongoski et al., 2013), in Himalaya at the Karakoram Fault (Klemperer et al., 2013), and along the DSF (Torfstein et al., 2013; Yuce et al., 2014; Inguaggiato et al., 2016). The He isotopic ratios measured in this study ranged from 1.30×10^{-6} to 1.38×10^{-6} (i.e., 0.937 to 0.990 R/Ra), which illustrates that most samples contain an atmospheric air component without signature of the mantle component (Fig. 9). Unlike the compositions of dissolved gases from the Amik Basin, which exhibit distinct crustal signatures (Yuce et al., 2014), most analyzed soil samples in this study are dominated by air

Table 3
Soil CO_2 flux observed in the Amik Basin and other tectonic areas of the world.

Location	Country	CO_2 flux (g/m^2/d)	Reference
Dead Sea Fault - population A	Turkey	0.8	This study
Dead Sea Fault - population B	Turkey	6.9	This study
Dead Sea Fault - population C	Turkey	26.7	This study
San Andreas Fault	USA	19	(Lewicki et al., 2003)
San Andreas Fault - Background	USA	13	(Lewicki et al., 2003)
Calaveras Fault	USA	56	(Lewicki et al., 2003)
Calaveras Fault - Background	USA	55	(Lewicki et al., 2003)
Arbia Fault (Italy)	Italy	78	(Etiope, 1999)
Arbia Fault	Italy	6.2	(Etiope, 1999)
Chukuo Fault	Taiwan	17	(Cheng, 2009)
Chukuo Fault - Background	Taiwan	7.1	(Cheng, 2009)

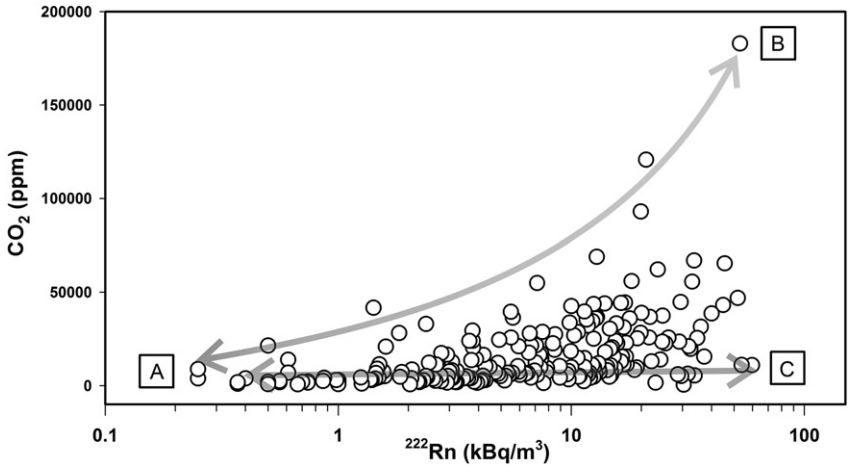

Fig. 8. Variation diagram of Rn versus CO_2 compositions of soil gas. At least three end members can be identified: (C) air component with low Rn and CO_2 concentrations, (B) deep source component with high Rn and CO_2 concentrations, (C) shallow source component with high Rn but low CO_2 concentrations.

composition as shown in the three-component plot (Fig. 9). Similar variation of the $^3He/^4He$ ratio in soil gas was also observed along the Chaochou fault zone in Taiwan, which is also a major left-lateral strike-slip fault with a high angle thrust fault plane (Fu et al., 2005), i.e., the gas has obviously been mixed with a crustal component and an atmospheric air component. Furthermore, since the mantle component has been ruled out based on He isotopic data, soil gas might migrate toward the surface through the fault/fracture zones from its deep crustal source.

A horizontal geochemical (soil gas) profile in the Amik Basin was chosen following the *E*-W directions (E 36.375° to E 36.40°, N 36.20° to N 36.61°). Rn and CO_2 concentrations, and CO_2 flux results are shown in Fig. 10. Some anomalous values above the calculated threshold (17 kBq/m^3 for Rn, 40,000 ppm for CO_2, and 16 g/m^2/d for CO_2 flux; see Fig. 4) can be found at specific positions along the profile. We observed that few high Rn concentration, CO_2 concentration, and CO_2 flux occurred at the same site, especially in correspondence with the location of the DSF zone. Anomalies in Rn concentration can also be observed at the eastern and western sides of the profile, which coincide with the Karasu Fault and the basin-bounding fault in the area. Assuming that those anomalous high concentration gases mainly come from deep-crustal sources through the faults/fractures zone, they can be explained well by the advection model, i.e., via CO_2 serving as the carrier gas to bring the trace gas, Rn, to the surface. Therefore, it can be inferred that those sites may be the surface trace of fault/fracture zones in this area. It is interesting to note that, however, some of the high concentration sample sites do not simultaneously exhibit both high Rn concentration, CO_2 concentration, and CO_2 flux. This suggests that there are, in addition to the deep-crustal source component, multiple sources for those high concentration gases. Gas sources of the studied samples have been discussed in the former section.

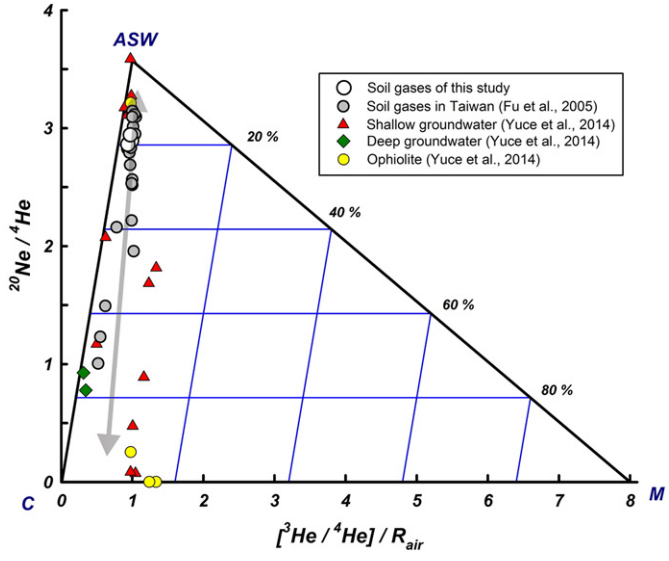

Fig. 9. Three-component plot of the He isotopes of representative soil gas samples. The results from groundwater and ophiolite samples around the Amik Basin and soil gas samples along the fault zone in Taiwan are also shown for comparison (data from Fu et al., 2005; Yuce et al., 2014). A: air; C: crust; M: mantle component.

Torfstein et al. (2013) pointed out a variable input of the mantle component on a constant crustal flux along the southernmost DSF segment whose carrier is mainly mantle CO_2 (Inguaggiato et al., 2016). This could suggest that the mantle-derived component in the DSF segment crosses the Amik Basin in the same way. Yuce et al. (2014) proposed that the deep mantle-type source reaches the surface by moving across the shallow-level fracture field of the active DSF, due to the regional degassing over that large area. Therefore, we suggest that the DSF zone plays the main role in the Amik Basin, influencing the degassing of the mantle and lower crust volatiles, as well as the release of gases trapped in the crustal blocks. Based on our results of soil gases, a mixing of a deep source with shallow components has not only been found close to the DSF zone, but also at the Karasu Fault and the Basin-bounding Fault at the eastern and western margins of the Amik Basin, respectively. Furthermore, the occurrence of degassing along the northeastern and southwestern borders of the Amik Basin can also be identified as two lineaments in the NW-SE direction. The Amik Basin can therefore be interpreted as another pull-apart basin within the DSF, comparable with the Ghab basin (Yurtmen et al., 2002; Seyrek et al., 2007, 2008). A sinistral displacement has occurred along the DSF system, which extended through the Amik Basin in the N-S direction and elongated the Amik Basin. The extended normal faults and the bounding faults were developed during the opening stage of the basin. Combined with the aforementioned, a relationship between soil gas degassing and the tectonic setting model of the study area could be constructed (Fig. 11a).

A schematic degassing model that summarizes the main origin and evolution of the gas components in the study area is shown in Fig. 11b. The shallow sources are characterized by low soil gas concentrations (population C in Fig. 8) and a gas phase composed of a mixture of atmospheric and CO_2-dominated near-surface gases. The widespread presence of high soil gas values was observed at the eastern side of the

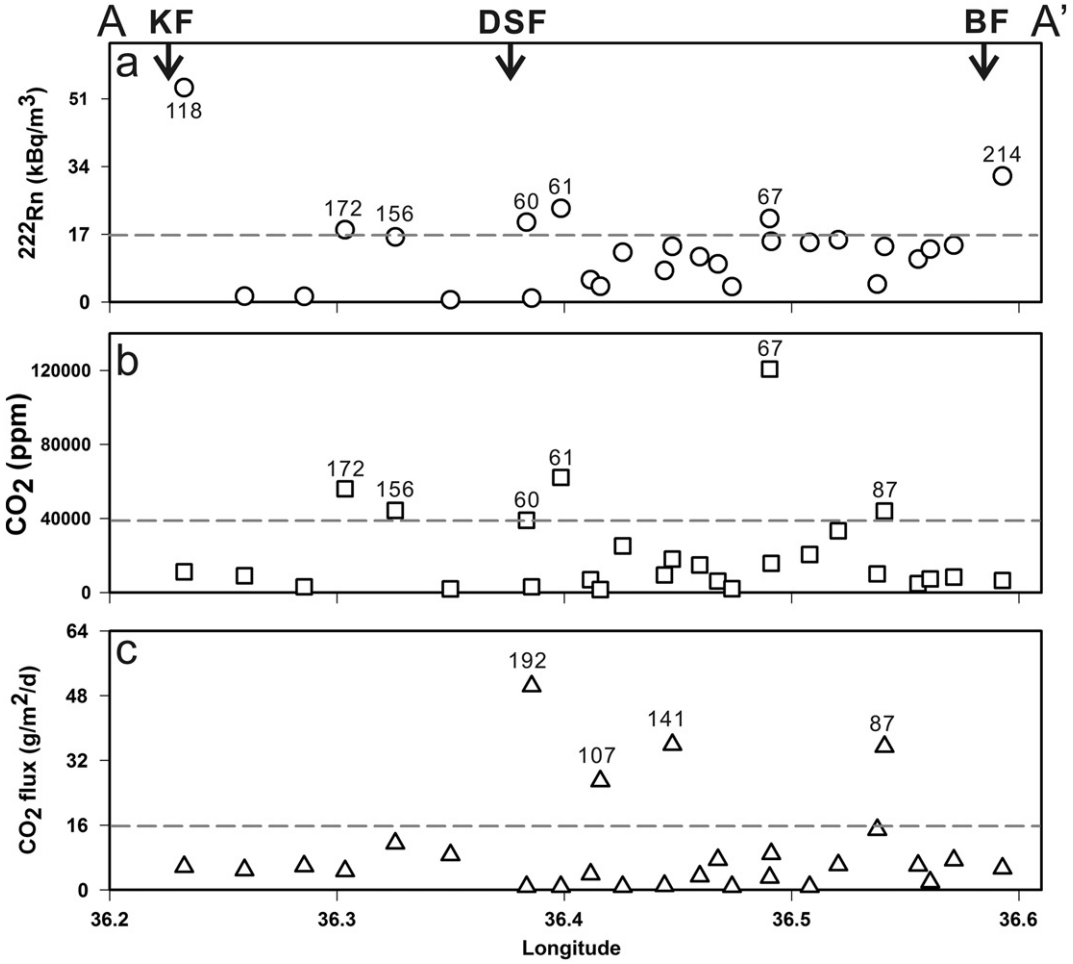

Fig. 10. Variations of Rn concentration, CO_2 concentration, and CO_2 flux of soil gases for the E-W profile in the Amik Basin (AA' in Fig. 1). The dashed line indicates the anomaly threshold of soil gas (see Fig. 4). KF: Karasu Fault; DSF: Dead Sea Fault; BF: basin-bounding fault.

DSF, and many high soil gas anomalies are distributed at specific locations around the margin of the Amik Basin. This suggests that the presence of fault/fractures such as the DSF, KF, and BF can provide the channel with gases migrating from the deep crust or mantle toward the surface (Fig. 11b). As is evidenced by the soil gas samples, high Rn concentrations are carried by high CO_2 concentrations, which occur along the fault (Figs. 5d and 8). In contrast, the low geochemical features of the soil gas samples collected from the western side of the DSF within the Amik Basin may be strongly influenced by the thick sediments that fill up the depocenter of the Amik Basin (Perinçek and Çemen, 1990). The presence of a multilayered aquifer system in the Amik Basin that enhances the gas dissolution process is also a possible reason (Yuce et al., 2014).

Hence, as shown in Fig. 12, a schematic model for the pull-apart basin based on soil gas observations was proposed. The anomalous soil Rn and CO_2 occur in three regions: (a) the outer boundary faults, (b) the DSF, and (c) the leakage edge of the pull-apart basin. The largest gas leakages around the Amik Basin occur at the leakage edge of the pull-apart basin, which is shown as a grey shadow in Fig. 12.

Our results confirm that effective gas migration from depth toward the surface occurs despite the strongly thick strata, sediments, and aquifer system of the Amik Basin. The geochemical features of the soil gas released in the study area highlight the variable extent of the mixing of gas species that come from shallow and deep sources. The soil gas technique can therefore be considered as a suitable tool for the exploration of buried faults and/or fractures, at least in the Amik Basin.

5. Summary

In summary, we studied the spatial anomalies of soil gas and examined the relationship between soil degassing and the distribution of faults/fractures in the Amik Basin, SE Turkey. The major findings of this study are listed below:

(1) In the present case, the results show that Rn concentration and CO_2 (flux and concentration) are reliable and sensitive indicators for tracing faults because spot or halo concentrations recorded on the fault trace are higher than the background values. Rn, CO_2, and CO_2 flux anomalies are distributed along the N-S and NW-SE trending faults in the study area, and are in good agreement with the DSF and the basin-bound fault of the Amik Basin, including the Karasu Fault.

Fig. 11. (a) Schematic diagram showing the relative distribution of gas emanation and the tectonic setting around the study area. Black arrows show the approximate relative movement of the fault; the red arrow indicates the extension direction of the study area; the yellow shadow indicates the high emanation area. (b) Schematic gas degassing model of the study area. The grey arrows indicate the atmospheric air; the green arrow indicates shallow source; the purple arrows show mantle or lower crust volatiles; the red arrow presents gas migrating upward along the deep-rooted faults of deep origin enriched in deep volatiles (mantle and crustal).

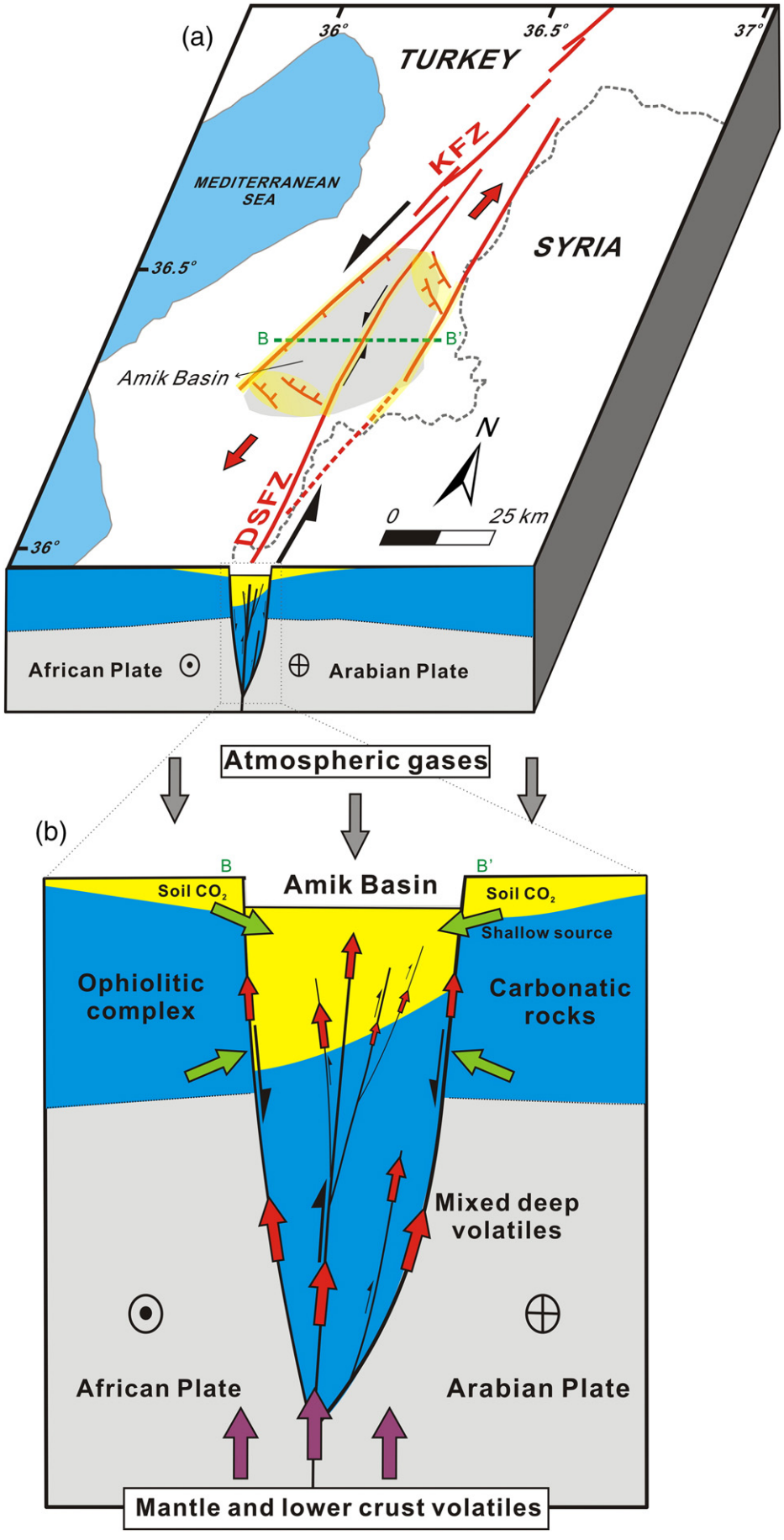
(a)
36°
36.5°
37°
TURKEY
KFZ
MEDITERRANEAN SEA
SYRIA
36.5°
B
B'
Amik Basin
N
DSFZ
0
25 km
36°
African Plate
Arabian Plate
Atmospheric gases
(b)
B
Amik Basin
B'
Soil CO2
Soil CO2
Shallow source
Ophiolitic complex
Carbonatic rocks
Mixed deep volatiles
African Plate
Arabian Plate
Mantle and lower crust volatiles

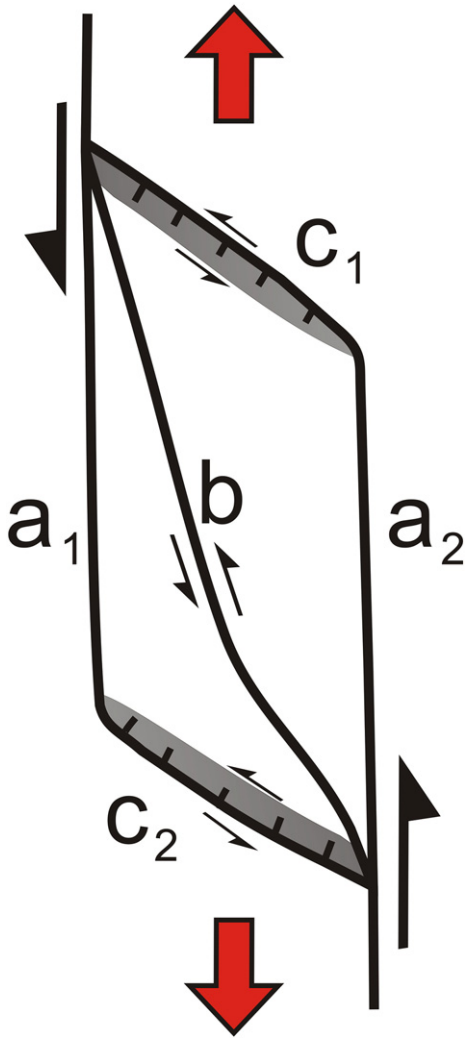

Fig. 12. A schematic model for the pull-apart basin based on observations: (a) a_1 (Karasu Fault) and a_2 are the outer boundary fault; (b) b is the DSF, and (c) c_1 and c_2 are the leakage edge of the pull-apart basin. The leakage edge c_1 and c_2 have a large Rn and CO_2 leakage.

(2) A deep crustal gas component exhibited high Rn and CO_2 concentrations, which are considered as good indicators for tracing deep faults/fractures in the area. In addition to Rn and CO_2 measurements, He isotopic ratios and $\delta^{13}C_{CO_2}$ of soil gases were determined to unearth probable buried faults and fractures zones and may be sensitive to the deep faults/fractures – similar to soil gas mixed with a crustal component and an atmospheric air component.

(3) The observed higher concentrations at fewer measurement sites in 2014 compared to earlier records in 2013 may be associated with the activity of the DSF. Continuous monitoring, therefore, is necessary to further clarify the relationship between soil gas variations and fault activities.

(4) As illustrated in Fig. 12, the Rn and CO_2 gas leakage occurs in three regions: (a) the outer boundary fault, (b) the DSF, and (c) the two leakage edge of the pull-apart basin. The largest gas leakage occurs at the leakage edge of the pull-apart basin.

Acknowledgments

This work was funded by the Scientific and Technological Research Council of Turkey (TUBITAK), project (COST) no. 111Y090. The research is also supported by grants MOST104-2119-M-001-004, MOST105-2811-M-001-010 and the Taiwan Earthquake Research Center (TEC), which is funded through the Ministry of Science and Technology (MOST). The TEC contribution number for this article is 00128. We thank Ms. Y.T. Lin for help with the He isotopes analysis. This paper is dedicated to co-author Prof. Tsanyao Frank Yang (TFY), who passed away on 12 March 2015. Born in 1961, TFY worked for many years at the Department of Geosciences, National Taiwan University (NTU), Taipei, Taiwan. His passion for research set new standards for all who worked with him. TFY will be greatly missed within the Earth science community, not only for his large scientific expertise, but also for his great personal qualities. The comments and suggestions of Fátima Viveiros, the editor Guodong Zheng, and one anonymous referee helped us improve the manuscript.

References

Al-Hilal, M., Mouty, M., 1994. Radon monitoring for earthquake prediction on Al-Ghab of Syria. Nucl. Geophys. 8, 291–299.
Astorri, F., Lombardi, S., Paoloni, F., 1999. Soil gas investigations over sulphide ore-bearing fractures - the Fontalcinaldo case study (Boccheggiano and Niccioleta mining district - southern Tuscany, Italy). Per. Mineral. 68 (2), 93–108.
Ballentine, C.J., Burgess, R., Marty, B., 2002. Tracing fluid origin, transport and interaction in the crust. Rev. Mineral. Geochem. 47:539–614. http://dx.doi.org/10.2138/rmg.2002.47.13.
Barka, A., Reilinger, R., 1997. Active tectonics of the Mediterranean region: deduced from GPS, neotectonic and seismicity data. Ann. Geofis. XI/3, 587–610.
Baubron, J.-C., Allard, P., Sabroux, J.-C., Tedesco, D., Toutain, J.-P., 1991. Soil gas emanations as precursory indicators of volcanic eruptions. J. Geol. Soc. Lond. 148, 571–576.
Baubron, J.C., Rigo, A., Toutain, J.P., 2002. Soil gas profiles as a tool to characterize active tectonic areas: The Jaut Pass example (Pyrenees, France). Earth Planet. Sci. Lett. 196, 69–81.
Beaubien, S.E., Ciotoli, G., Lombardi, S., 2003. Carbon dioxide and radon gas hazard in the Albani Hills area (Central Italy). J. Volcanol. Geotherm. Res. 123, 63–80.
Belt, J.Q., Rice, G.K., 2002. Application of statistical quality control measures for near-surface geochemical petroleum exploration. Comput. Geosci-UK 28, 243–260.
Blunt, M., Fayers, F.J., Orr, F.M., 1993. Carbon dioxide in enhanced oil recovery. Energy Convers. Manag. 34, 1197–1204.
Boulton, S., Robertson, A.H.F., Ünlügenç, U.C., 2006. Tectonic and sedimentary evolution of the Cenozoic Hatay Graben, Southern Turkey: a two-phase model for graben formation. In: Robertson, A.H.F., Mountrakis, D. (Eds.), Tectonic Development of the Eastern Mediterranean Region. Geol. Soc. London Spec. Publ 260:pp. 613–634. http://dx.doi.org/10.1144/GSL.SP.2006.260.01.26.
Boyle, R.W., 2013. Geochemical Prospecting for Thorium and Uranium Deposits. Elsevier.
Bridgland, D.R., Westaway, R., Abou Romieh, M., Candy, I., Daoud, M., Demir, T., Galiatsatos, N., Schreve, D.C., Seyrek, A., Shaw, A., White, T.S., Whittaker, J., 2012. The River Orontes in Syria and Turkey: downstream variation of fluvial archives in different crustal blocks. Geomorphology 165-166, 25–49.
Bunzl, K., Ruckerbauer, F., Winkler, R., 1998. Temporal and small-scale spatial variability of ^{222}Rn gas in a soil with a high gravel content. Sci. Total Environ. 220, 157–166.
Burton, M., Neri, M., Condarelli, D., 2004. High spatial resolution radon measurements reveal hidden active faults on Mt. Etna. Geophys. Res. Lett. 31 (7), 1–4.
Butt, C.R.M., Gole, M.J., 1986. Groundwater helium surveys in mineral exploration in Australia. J. Geochem. Explor. 25, 309–344.
Çapan, U.Z., Vidal, P., Cantagrel, J.M., 1987. K-Ar, Nd, Sr and Pb isotopic study of the quaternary volcanism in Karasu rift (Hatay), N-end of Dead Sea rift zone in SE Turkey. H.Ü. Yerbilimleri 14, 165–178.
Capasso, G., Favara, R., Grassa, F., Inguaggiato, S., Longo, M., 2005. On-line technique for preparation and measuring stable carbon isotope of total dissolved inorganic carbon in water samples (δ^{13}CTDIC). Ann. Geophys. 48:159–166. http://dx.doi.org/10.4401/ag-3190.
Chaimov, T.A., Barazangi, M., 1990. Crustal shortening in the Palmyride Fold Belt, Syria, and implications for movement along Dead Sea fault system. Tectonics 9, 1369–1386.
Cheng, C.Y., 2009. Emission Flux of CO_2 Through an Active Fault Zone and Estimation of CO_2 Reservoir in SW Taiwan. (MS Thesis, Inst.). Geosciences. National Taiwan Univ (77 pp. (in Chinese with English abstract)).
Cheng, Q., Agterberg, F.P., Ballantyne, S.B., 1994. The separation of geochemical anomalies from background by fractal methods. J. Geochem. Explor. 51, 109–130.
Chiodini, G., Cioni, R., Guidi, M., Raco, B., Marini, L., 1998. Soil CO_2 flux measurements in volcanic and geothermal areas. Appl. Geochem. 13, 543–552.
Chyi, L.L., Chou, C.Y., Yang, T.F., Chen, C.-H., 2001. Continuous radon measurements in faults and earthquake precursor pattern recognition. West. Pac. Earth Sci. 1 (2), 43–72.
Chyi, L.L., Quick, T.J., Yang, F.T., Chen, C.H., 2005. Soil gas radon spectra and earthquakes. Terr. Atmos. Ocean. Sci. 16, 763–774.
Ciotoli, G., Guerra, M., Lombardi, E., Vittori, E., 1998. Soil gas survey for tracing seismogenic faults: a case study in the Fucino basin, Central Italy. J. Geophys. Res. 103, 23781–23794.
Ciotoli, G., Etiope, G., Guerra, M., Lombardi, S., 1999. The detection of concealed faults in the Ofanto Basin using the correlation between soil gas fracture surveys. Tectonophysics 301, 321–332.
Ciotoli, G., Lombardi, S., Annunziatellis, A., 2007. Geostatistical analysis of soil gas data in a high seismic intermontane basin: Fucino Plain, central Italy. J. Geophys. Res. 112, B05407. http://dx.doi.org/10.1029/2005JB004044.
Ciotoli, G., Bigi, S., Tartarello, C., Sacco, P., Lombardi, S., Ascione, A., Mazzoli, A., 2014. Soil gas distribution in the main coseismic surface rupture zone of the 1980, Ms = 6.9, Irpinia Earthquake (southern Italy). J. Geophys. Res. 119:2440–2461. http://dx.doi.org/10.1002/2013JB010508.
Corazza, E., Magro, G., Pieri, S., Rossi, U., 1993. Soil gas survey in the geothermal area of Bolsena Lake (Vulsini Mountains, central Italy). Geothermics 22, 201–214.

D'Alessandro, W., Bellomo, S., Brusca, L., Fiebig, J., Longo, M., Martelli, M., Pecoraino, G., Salerno, F., 2009. Hydrothermal methane fluxes from the soil at Pantelleria island (Italy). J. Volcanol. Geotherm. Res. 187:147–157. http://dx.doi.org/10.1016/j.jvolgeores.2009.08.018.

D'Alessandro, W., Brusca, L., Kyriakopoulos, K., Bellomo, S., Calabrese, S., 2014. A geochemical traverse along the "Sperchios Basin — Evoikos Gulf" Graben (Central Greece): origin and evolution of the emitted fluids. Mar. Pet. Geol. http://dx.doi.org/10.1016/j.marpetgeo.2013.12.011.

Dilek, Y., Thy, P., 2009. Island arc tholeiite to boninitic melt evolution of the Cretaceous Kizildag (Turkey) ophiolite: Model for multi-stage early arc-forearc magmatism in Tethyan subduction factories. Lithos 113:68–87. http://dx.doi.org/10.1016/j.lithos.2009.05.044.

Dooley, T., McClay, K., 1997. Analog modelling of pull-apart basins. Am. Assoc. Pet. Geol. Bull. 81, 1804–1826.

El-Arabi, A.M., Abbady, A., Ahmed, N.K., Michel, R., El-Kamel, A.H., Abbady, A.G.E., 2006. Assessment of radon-222 concentrations and exhalation rates of rocks and building materials. Indian J. Pure Appl. Phys. 44, 287–291.

Erdik, M., Aydinoglu, N., Pinar, A., Kalafat, D., 1997. Hatay Deprem Raporu. Kandilli Obs, Istanbul.

Etiope, G., 1999. Subsoil CO_2 and CH_4 and their advective transfer from faulted grassland to the atmosphere. J. Geophys. Res. 104, 16889–16894.

Etiope, G., 2015. Natural gas seepage. The Earth's Hydrocarbon Degassing. Springer, p. 199.

Etiope, G., Lombardi, S., 1995. Evidence for radon transport by carrier gas through faulted clays in Italy. J. Radioanal. Nucl. Chem. 193, 291–300.

Etiope, G., Martinelli, G., 2002. Migration of carrier and trace gases in the geosphere: An overview. Phys. Earth Planet. Inter. 129, 185–204.

Freund, R., Zak, I., Garfunfel, Z., 1968. On the age and rate of sinistral movement along the Dead Sea rift. Nature 220, 253–255.

Fu, C.C., Yang, T.F., Walia, V., Chen, C.-H., 2005. Reconnaissance of soil gas composition over the buried fault and fracture zone in southern Taiwan. Geochem. J. 39, 427–439.

Fu, C.C., Yang, T.F., Du, J., Walia, V., Liu, T.K., Chen, Y.G., Chen, C.-H., 2008. Variations of helium and radon concentrations in soil gases from an active fault zone in southern Taiwan. Radiat. Meas. 43, 348–352.

Fu, C.C., Yang, T.F., Walia, V., Liu, T.K., Lin, S.J., Chen, C.-H., Hou, C.S., 2009. Variations of soil-gas composition around the active Chihshang fault in a plate suture zone, eastern Taiwan. Radiat. Meas. 44, 940–944.

Fu, C.C., Wang, P.K., Lee, L.C., Lin, C.H., Chang, W.Y., Giuliani, G., Ouzounov, D., 2015. Temporal variation of gamma rays as a possible precursor of earthquake in the Longitudinal Valley of eastern Taiwan. J. Asian Earth Sci. 114 (2), 362–372.

Garfunkel, Z., 1981. Internal structure of the Dead Sea leaky transform (rift) in relation to plate kinematics. Tectonophysics 80, 81–108.

Gole, M.J., Butt, C.R.M., Snelling, A.A., 1986. A groundwater helium survey of the Koongarra uranium deposits, Pine Creek Geosyncline, Northern Territory. Uranium 2, 343–360.

Gomez, F., Karam, G., Khawlie, M., McClusky, S., Vernant, P., Reilinger, R., Jaafar, R., Tabet, C., Khair, K., Barazangi, M., 2007. Global positioning system measurements of strain accumulation and slip transfer through the restraining bend along the Dead Sea fault system in Lebanon. Geophys. J. Int. 168, 1021–1028.

Guerra, M., Lombardi, S., 2001. Soil gas method for tracing neotectonic faults in clay basins: the Pisticci field (Southern Italy). Tectonophysics 339 (3), 511–522.

Gülec, N., Hilton, D.R., Mutlu, H., 2002. Helium isotope variations in Turkey: relationship to tectonics, volcanism and recent seismic activities. Chem. Geol. 187, 129–142.

Heiligmann, M., Stix, J., Williams-Jones, G., Lollar, B.S., Gustavo Garzon, V., 1997. Distal degassing of radon and carbon dioxide on Galeras volcano, Colombia. J. Volcanol. Geotherm. Res. 77, 267–283.

Hempton, M.R., 1987. Constraints on Arabian plate motion and extensional history of the Red Sea. Tectonics 6, 687–705.

Hinkle, M., 1994. Environmental conditions affecting concentrations of He, CO_2, O_2 and N_2 in soil gases. Appl. Geochem. 9, 53–63.

Hoefs, J., 2004. Stable Isotope Geochemistry. Springer, Berlin, pp. 31–76 (Chapt. 2).

Hong, W.L., Yang, T.F., Walia, V., Lin, S.J., Fu, C.C., Chen, Y.G., Sano, Y., Chen, C.-H., Wen, K.L., 2010. Nitrogen as the carrier gas for helium emission along an active fault in NW Taiwan. Appl. Geochem. 25, 593–601.

Iakovleva, V.S., Ryzhakova, N.K., 2003. Spatial and temporal variations of radon concentration in soil air. Radiat. Meas. 36, 385–388.

Inan, S., Akgül, T., Seyis, C., Saatçýlar, R., Baykut, S., Ergintav, S., Bas, M., 2008. Geochemical monitoring in the Marmara region (NW Turkey): A search for precursors of seismic activity. J. Geophys. Res. 113, 1–4.

Inceoz, M., Baykara, O., Aksoy, E., Dogru, M., 2006. Measurements of soil gas radon in active fault systems: a case study along the North and East Anatolian fault systems in Turkey. Radiat. Meas. 41 (3), 349–353.

Inguaggiato, C., Censi, P., D'Alessandro, W., Zuddas, P., 2016. Geochemical characterisation of gases along the dead sea rift: Evidences of mantle-CO_2 degassing. J. Volcanol. Geotherm. Res. 320, 50–57.

Ioannides, K., Papachristodoulou, C., Stamoulis, K., Karamanis, D., Pavlides, S., Chatzipetros, A., Karakala, E., 2003. Soil gas radon: a tool for exploring active fault zones. Appl. Radiat. Isot. 59, 205–213.

Italiano, F., Sasmaz, A., Yuce, G., Okan, O.O., 2013. Thermal fluids along the East Anatolian Fault Zone (EAFZ): geochemical features and relationships with the tectonic setting. Chem. Geol. 339:103–114. http://dx.doi.org/10.1016/j.chemgeo.2012.07.027.

Kafadar, K., Spiegelman, C.H., 1986. An alternative to ordinary Q-Q plots: conditional Q-Q plots. Pub. Comput. Stat. Data An. 4 (1986), 167–184.

Karabacak, V., Altunel, E., 2013. Evolution of the northern Dead Sea fault zone in southern Turkey. J. Geodyn. 65, 282–291.

Karabacak, V., Altunel, E., Meghraoui, M., Akyüz, H.S., 2010. Field evidences from northern Dead Sea fault zone (South Turkey): new findings for the initiation age and slip rate. Tectonophysics 480, 172–182.

Kasapoglu, E.K., 1987. Seismotectonic characteristics of Eastern Mediterranean: a finite elements analysis. H.Ü. Yerbilimleri 14, 309–317.

King, C.Y., 1980. Episodic radon changes in subsurface soil gas along active faults and possible relation to earthquakes. J. Geophys. Res. 85, 3065–3078.

King, C.Y., King, B.S., Evans, W.C., Zhang, W., 1996. Spatial radon anomalies on active faults in California. Appl. Geochem. 11 (4), 497–510.

Kiratzi, A.A., 1993. A study of the active crustal deformation of the North and East Anatolian fault zones. Tectonophysics 225, 191–203.

Klemperer, S.L., Kennedy, B.M., Sastry, S.R., Makovsky, Y., Harinarayana, T., Leech, M.L., 2013. Mantle fluids in the Karakoram fault: helium isotope evidence. Earth Planet. Sci. Lett. 366:59–70. http://dx.doi.org/10.1016/j.epsl.2013.01.013.

Kulongoski, J.T., Hilton, D.R., Barry, P.H., Esser, B.K., Hillegonds, D., Belitz, K., 2013. Volatile fluxes through the Big Bend section of the San Andreas Fault, California: helium and carbon-dioxide systematics. Chem. Geol. 339:92–102. http://dx.doi.org/10.1016/j.chemgeo.2012.09.007.

Kuran, U., 1980. The location, magnitude and long-term time prediction of damaging earthquakes along the Anatolian faults and Levant coast. Bull. Geol. Congress Turkey 2, 151–163.

Lewicki, J.L., Evans, W.C., Hilley, G.E., Sorey, M.L., Rogie, J., Brantley, S.L., 2003. Shallow soil CO_2 flow along the San Andreas and Calaveras Faults, California. J. Geophys. Res. 108 (B4): 2187. http://dx.doi.org/10.1029/2002JB002141.

Lombardi, S., Voltattorni, N., 2010. Rn, He and CO_2 soil-gas geochemistry for the study of active and inactive faults. Appl. Geochem. 25, 1206–1220.

Lyberis, N., Yürür, T., Chorowicz, J., Kasapoglu, E., Gündogdu, N., 1992. The East Anatolian fault: an oblique collisional belt. Tectonophysics 204, 1–15.

Mahmoud, S., Reilinger, R., McClusky, S., Vernant, P., Tealeb, A., 2005. GPS evidence for northward motion of the Sinai block: Implications for E. Mediterranean tectonics. Earth Planet. Sci. Lett. 238:217–224. http://dx.doi.org/10.1016/j.epsl.2005.06.063.

McClusky, S.C., Balassanian, S., Barka, A., Ergintav, S., Georgie, I., Gurkan, O., Hamburger, M., Hurst, K., Kahle, H., Kastens, K., Kekelidse, G., King, R., Kotzev, V., Lenk, O., Mahmout, S., Mishin, A., Nadaria, M., Ouzounis, A., Paradisissis, D., Peter, Y., Pirilepin, M., Reilinger, R.E., Sanli, I., Seeger, H., Teableb, A., Toksöz, N., Veis, V., 2000. Global positioning system constraints on plate kinematics and dynamics in the eastern Mediterranean Caucasus. J. Geophys. Res. 105, 5695–5719.

McClusky, S., Reilinger, R., Mahmoud, S., Sari, D.B., Tealeb, A., 2003. GPS constraints on Africa (Nubia) and Arabia plate motion. Geophys. J. Int. 155, 126–138.

McKenzie, D.P., 1972. Active tectonics of the Mediterranean region. Geophys. J. R. Astron. Soc. 30, 109–185.

Meghraoui, M., Gomez, F., Sbeinati, R., Woerd, J., Mouty, M., Darkal, A.N., Radwan, Y., Layyous, I., Al Najjar, H., Darawcheh, R., Hijazi, F., Al-Ghazzi, R., Barazangi, M., 2003. Evidence for 830 years of seismic quiescence from palaeoseismology, archaeoseismology and historical seismicity along the Dead Sea fault in Syria. Earth Planet. Sci. Lett. 210, 35–52.

Meghraoui, M., Çakır, Z., Masson, F., Mahmood, Y., Ergintav, S., Alchalbi, A., Inan, S., Daoud, M., Yonlu, O., Altunel, E., 2011. Kinematic modelling at the triple junction between the Anatolian, Arabian, African plates (NW Syria and in SE Turkey). Geophys. Res. Abstr. 13, EGU2011–EGU12599.

Muehlberger, R.W., 1981. The splintering of the Dead Sea fault zone in Turkey. H. U. Yerbilimleri Bull. 8, 123–130.

Perinçek, D., Çemen, Í., 1990. The structural relationship between the East Anatolian and Dead Sea fault zones in southeastern Turkey. Tectonophysics 172, 331–340.

Phuong, N.K., Harijoko, A., Itoi, R., Unoki, Y., 2012. Water geochemistry and soil gas survey at Ungaran geothermal field, central Java, Indonesia. J. Volcanol. Geotherm. Res. 229, 23–33.

Poreda, R., Craig, H., 1989. Helium isotope ratios in Circum-Pacific volcanic arcs. Nature 338, 473–478.

Pulinets, S.A., Dunajecka, M.A., 2007. Specific variations of air temperature and relative humidity around the time of Michoacan earthquake M8.1 Sept. 19, 1985 as a possible indicator of interaction between tectonic plates. Tectonophysics 431, 221–230.

Quennell, A.M., 1958. The structural and geomorphic evolution of the Dead Sea rift. Q. J. Geol. Soc. Lond. 114, 1–24.

Reilinger, R., McClusky, S.C., Oral, M.B., King, W., Toksöz, M.N., 1997. Global positioning, system measurements of present-day crustal movements in the Arabia-Africa-Eurasia plate collision zone. J. Geophys. Res. 102, 9983–9999.

Reilinger, R., McClusky, S., Vernant, P., Lawrence, S., Ergintav, S., Cakmak, R., Ozener, H., Kadirov, F., Guliev, I., Stepanyan, R., Nadariya, M., Hahubia, G., Mahmoud, S., Sakr, K., Ar Rajehi, A., Paradissis, D., Al-Aydrus, A., Prilepin, M., Guseva, T., Evren, E., Dmitrotsa, A., Filikov, S.V., Gomez, F., Al-Ghazzi, R., Karam, G., 2006. GPS constraints on continental deformation in the Africa-Arabia-Eurasia continental collision zone and implications for the dynamics of plate interactions. J. Geophys. Res. 111 (B5), B05411.

Robertson, A.H.F., 1998. Tectonic significance of the Eratosthenes Seamount: a continental fragment in the process of collision with a subduction zone in the E Mediterranean (ODP Leg 160). Tectonophysics 298 (1–3), 63–82.

Rodgers, D., 1980. Analysis of pull-apart basin development produced by en echelon strike-slip faults. Spec. Publ. Assoc. Sediment. 4, 27–41.

Rojay, B., Heimann, A., Toprak, V., 2001. Neotectonic and volcanic characteristics of the Karasu fault zone (Anatolia, Turkey): the transition zone between the Dead Sea transform and the East Anatolian fault zone. Geodin. Acta 14, 197–212.

Sano, Y., Wakita, H., 1985. Geographical distribution of $^3He/^4He$ in Japan: implications for arc tectonics and incipient magmatism. J. Geophys. Res. 90, 8729–8741.

Saroglu, F., Emre, O., Kuşçu, I., 1992. The East Anatolian fault zone of Turkey. Ann. Tectonicae 6, 99–125.

Sengör, A.M.C., Yilmaz, Y., 1981. Tethyan evolution of Turkey: a plate tectonic approach. Tectonophysics 75, 181–241.

Sensintaffar, E.L., Windham, S.T., 1990. Calibration of scintillation cellsfor radon-222 measurements at the U.S. Environmental Protection Agency. J. Res. Natl. Inst. Stand. Technol. 95, 143–145.

Seyrek, A., Demir, T., Pringle, M., Yurtmen, S., Westaway, R., Beck, A., Rowbotham, G., 2007. Kinematics of the Amanos Fault, southern Turkey, from Ar-Ar dating of offset Pleistocene basalt flows: transpression between the African and Arabian plates. In: Cunningham, W.D., Mann, P. (Eds.), Tectonics of Strike-slip Restraining and Releasing Bends. Geological Society, London, Special Publication Vol. 290, pp. 255–284.

Seyrek, A., Demir, T., Pringle, M., Yurtmen, S., Westaway, R., Bridgland, D., Beck, A., Rowbotham, G., 2008. Late Cenozoic uplift of the Amanos Mountains and incision of the Middle Ceyhan river gorge, southern Turkey; Ar-Ar dating of the Düziçi basalt. Geomorphology 97, 321–355.

Swakon, J., Kozak, K., Paszkowski, M., Gradzinski, R., Loskiewcz, J., Mazur, J., Janik, M., Bogaz, J., Horwacik, T., Olko, P., 2005. Radon concentration in soil gas around local disjunctive tectonic zones in the Krakow area. J. Environ. Radioact. 78, 137–149.

Tansi, C., Tallarico, A., Iovine, G., Folino-Gallo, M., Falcone, G., 2005. Interpretation of radon anomalies in seismotectonic and tectonicgravitational settings: The south-eastern Crati graben (northern Calabria, Italy). Tectonophysics 396, 181–193.

Tatar, O., Piper, J.D.A., Gürsoy, H., Heimann, A., Koçbulut, F., 2004. Neotectonic deformation in the transition zone between the Dead Sea Transform and the East Anatolian Fault Zone, southern Turkey: a palaeomagnetic study of the Karasu Rift volcanism. Tectonophysics 385, 17–43.

Torfstein, A., Hammerschmidt, K., Friedrichsen, H., Starinsky, A., Garfunkel, Z., Kolodny, Y., 2013. Helium isotopes in Dead Sea transform waters. Chem. Geol. 352:188–201. http://dx.doi.org/10.1016/j.chemgeo.2013.06.008.

Toutain, J.P., Baubron, J.C., 1999. Gas geochemistry and seismotectonics: a review. Tectonophysics 304, 1–27.

Toutain, J.P., Baubron, J.C., Le Bronec, J., Allard, P., Briole, P., Marty, B., Miele, G., Tedesco, D., Luongo, G., 1992. Continuous monitoring of distal gas emanations at Vulcano, southern Italy. Bull. Volcanol. 54, 147–155.

Trique, M., Richon, P., Avouac, J.P., Sabroux, J.C., 1999. Radon emanation and electric potential variations associated with transient deformation near reservoir lakes. Nature 399, 137–141.

Virk, H.S., Singh, B., 1993. Radon anomalies in soil-gas and groundwater as earthquake precursor phenomena. Tectonophysics 227, 215–224.

Walia, V., Su, T.C., Fu, C.C., Yang, T.F., 2005a. Spatial variations of radon and helium concentration in soil gas across Shan-Chiao fault, Northern Taiwan. Radiat. Meas. 40, 513–516.

Walia, V., Virk, H.S., Yang, T.F., Mahajah, S., Walia, M., Bajwa, B.S., 2005b. Earthquake prediction studies using Radon as a precursor in N-W Himalayas, India: A case study. Terr. Atmos. Ocean. Sci. 16, 775–804.

Walia, V., Mahajah, S., Kumar, A., Singh, S., Bajwa, B.S., Dhar, S., Yang, T.F., Walia, M., Bajwa, B.S., 2008. Fault delineation study using soil-gas method in Dharamsala area, NW Himalayas, India. Radiat. Meas. 43, 337–342.

Walia, V., Lin, S.J., Fu, C.C., Yang, T.F., Hong, W.L., Wen, K.L., Chen, C.-H., 2010. Soil-gas monitoring: a tool for fault delineation studies along Hsinhua Fault (Tainan), southern Taiwan. Appl. Geochem. 25, 602–607.

Walia, V., Yang, T.F., Lin, S.J., Kumar, A., Fu, C.C., Chiu, J.M., Chang, H.H., Wen, K.L., Chen, C.-H., 2013. Temporal variation of soil gas compositions for earthquake surveillance in Taiwan. Radiat. Meas. 50, 154–159.

Washington, J.W., Rose, A.W., 1992. Temporal variability of radon concentration in the interstitial gas of soils in Pennsylvania. J. Geophys. Res. 97, 9145–9159.

Westaway, R., 1994. Present day kinematics of the Middle East and Eastern Mediterranean. J. Geophys. Res. 99, 12071–12090.

Westaway, R., 2004. Kinematic consistency between the Dead Sea fault zone and the Neogene and Quaternary left-lateral faulting in SE Turkey. Tectonophysics 391, 203–237.

Yang, T.F., Chen, C.-H., Tien, R.L., Song, S.R., Liu, T.K., 2003a. Remnant magmatic activity in the Coastal Range of East Taiwan after arc-continent collision: fission-track date and $^{3}He/^{4}He$ ratio evidence. Radiat. Meas. 36, 343–349.

Yang, T.F., Chou, C.Y., Chen, C.-H., Chyi, L.L., Jiang, J.H., 2003b. Exhalation of radon and its carrier gases in SW Taiwan. Radiat. Meas. 36, 425–429.

Yang, T.F., Lan, T.F., Lee, H.F., Fu, C.C., Chuang, P.C., Lo, C.H., Chen, C.-H., Chen, C.T.A., Lee, C.S., 2005a. Gas compositions and helium isotopic ratios of fluid samples around Kueishantao, NE offshore Taiwan and its tectonic implications. Geochem. J. 39, 469–480.

Yang, T.F., Walia, V., Chyi, L.L., Fu, C.C., Chen, C.-H., Liu, T.K., Song, S.R., Lee, C.Y., Lee, M., 2005b. Variations of soil radon and thoron concentrations in a fault zone and prospective earthquakes in SW Taiwan. Radiat. Meas. 40, 496–502.

Yang, T.F., Fu, C.C., Walia, V., Chen, C.-H., Chyi, L.L., Liu, T.K., Song, S.R., Lee, M., Lin, C.W., Lin, C.C., 2006. Seismo-geochemical variations in SW Taiwan: multi-parameter automatic gas monitoring results. Pure Appl. Geophys. 163 (4), 693–709.

Yuce, G., Italiano, F., D'Alessandro, W., Yalcin, T.H., Yasin, D.U., Gulbay, A.H., Ozyurt, N.N., Rojay, B., Karabacak, V., Bellomo, S., Brusca, L., Yang, T.F., Fu, C.C., Lai, C.W., Ozacar, A., Walia, V., 2014. Origin and interactions of fluids circulating over the Amik Basin (Hatay-Turkey) and relationships with the hydrologic, geologic and tectonic settings. Chem. Geol. 388, 23–39.

Yurtmen, S., Guillou, H., Westaway, R., Rowbotham, G., Tatar, O., 2002. Rate of strike-slip motion on the Amanos fault (Karasu Valley, southern Turkey) constrained by K-Ar dating and geochemical analysis of Quaternary basalts. Tectonophysics 344, 207–246.

Yürür, T., Chorowicz, J., 1998. Recent volcanism, tectonics and plate kinematics near the junction of the African, Arabian and Anatolian plates in the eastern Mediterranean. J. Volcanol. Geotherm. Res. 85, 1–15.

Zhou, X., Du, J., Chen, Z., Cheng, J., Tang, Y., Yang, L., Xie, C., Cui, Y., Liu, L., Yi, L., Li, Y., 2010. Geochemistry of soil gas in the seismic fault zone produced by the Wenchuan Ms 8.0 earthquake, southwestern China. Geochem. Trans. 11 (5):1–10. http://dx.doi.org/10.1186/1467-4866-11-5.